A comprehensive process-based model for Arctic coastal erosion

Mohammad Akhsanul Islam[1] and Raed Lubbad[1]

[1]Norwegian University of Science and Technology

November 22, 2022

Abstract

In recent years, various models have been developed to describe Arctic coastal erosion. Many models are process-based, simulating multiple physical processes and combining them interactively to resemble Arctic coastal erosion. One limitation of the current process-based models is the difficulties in including the hydrodynamic forces. The morphological changes by the hydrodynamics are either simplified or simulated by some empirical relation. The reason for excluding detailed hydrodynamic forcing is the absence of thermal energy conservation in the systems of equations inside the available software. Most hydrodynamic models are designed considering the warmer climate, where waves, tides and storm surges cause changes in morphology. The available models cannot be applied where permafrost is a significant environmental parameter. This paper explains a methodology that allows us to use the models designed for warmer climates to simulate Arctic coastal erosion. The open-source software XBeach is used to simulate the waves, sediment transport and morphological changes. We developed different submodules for the processes related to permafrost thawing-freezing, slumping, wave-cut niche, bluff failure, etc. The submodules are coupled with the XBeach following a workflow where ice concentration, storm surge and bluff collapse work as an on-off switch. The submodules communicate with each other at three-hour intervals. The input parameters of the model are calibrated with field measurements. The model is then validated by another set of mutually exclusive field measurements under different geological conditions. The model can simulate the short term (one year) and long term (a few years) with the same level of fidelity.

A comprehensive process-based model for Arctic coastal erosion

Mohammad Akhsanul Islam[1]

Raed Lubbad[1]

[1]Department of Civil and Environmental Engineering, Norwegian University of Science and Technology (NTNU).

Key Points:

- A process-based comprehensive model to simulate Arctic coastal erosion is developed, including the hydrodynamic forcing.
- The open source software XBeach is modified and coupled with in house modules to simulate Arctic coastal erosion.
- The model is calibrated and validated using field measurements for both short-term and long-term simulation.

Corresponding author: Mohammad Akhsanul Islam, `mohammad.a.islam@ntnu.no`

Abstract

In recent years, various models have been developed to describe Arctic coastal erosion. Many models are process-based, simulating multiple physical processes and combining them interactively to resemble Arctic coastal erosion. One limitation of the current process-based models is the difficulties in including the hydrodynamic forces. The morphological changes by the hydrodynamics are either simplified or simulated by some empirical relation. The reason for excluding detailed hydrodynamic forcing is the absence of thermal energy conservation in the systems of equations inside the available software. Most hydrodynamic models are designed considering the warmer climate, where waves, tides and storm surges cause changes in morphology. The available models cannot be applied where permafrost is a significant environmental parameter. This paper explains a methodology that allows us to use the models designed for warmer climates to simulate Arctic coastal erosion. The open-source software XBeach is used to simulate the waves, sediment transport and morphological changes. We developed different submodules for the processes related to permafrost thawing-freezing, slumping, wave-cut niche, bluff failure, etc. The submodules are coupled with the XBeach following a workflow where ice concentration, storm surge and bluff collapse work as an on-off switch. The submodules communicate with each other at three-hour intervals. The input parameters of the model are calibrated with field measurements. The model is then validated by another set of mutually exclusive field measurements under different geological conditions. The model can simulate the short term (one year) and long term (a few years) with the same level of fidelity.

Plain Language Summary

Arctic coasts typically consist of permafrost rich bluffs at the end of the narrow beach. The presence of permafrost fundamentally changes the morphodynamics of the coast and warrants a special treatment while modelling the Arctic coastal erosion. Currently available process-based models are very site specific. They cannot be applied to the Arctic coasts, where the erosion mechanism is a mix of mechanical driven (thermoabrasion) and thermal driven (thermodenudation). We modified XBeach, open-source software and coupled it with our in-house modules to simulate Arctic coastal erosion with high fidelity. We developed a comprehensive model which combines a detailed simulation of permafrost thawing and the effect of hydrodynamic (wave, tide, currents) . The model is calibrated and validated using field data from one Arctic coast in Kara Sea, Russia. The simulation results are in good agreement with the field measurements. The numerical model can predict the short term and long term erosion.

1 Introduction

Approximately one-third of the coast worldwide consists of permafrost, for which the average retreat rate is close to 0.5 metres per year (Lantuit et al., 2012). The number of open-sea days in the Arctic is increasing rapidly (Overeem et al., 2011a). The annual retreat of the coastline along Alaska in the Beaufort Sea is 1.7 m per year (A. E. Gibbs & Richmond, 2015). In recent decades, coastal retreat along the Kara Sea has been measured between 1 and 1.7 metres per year (Isaev et al., 2019). The observed annual maximum retreats along the Alaskan coast were approximately 22 metres for the years 2007, 2012 and 2016 (A. Gibbs et al., 2018; B. M. Jones et al., 2009; B. Jones et al., 2018a). Other Arctic coasts are retreating at the same level of magnitude. The most significant erosion along the coast of the Kara Sea was observed to be 19.6 metres in 2010-11(Ogorodov et al., 2020).

The environmental changes due to the warming of the climate are triggering more significant coastal erosion in the Arctic (Rowland et al., 2010). The seawater temperature anomalies reached 5°C in the Arctic Ocean (Steele et al., 2008). The frequency and intensity of storms during summer are also expected to increase (Holland-Bartels & Pierce, 2011). Increased thawing of the permafrost inside the coastal bluffs leads to slumping and, consequently, loss of mass along the Arctic coast. On the other hand, the sea ice extent is shrinking, which enables longer fetches to generate larger waves (Overeem et al., 2011b, 2011c). A longer open sea season also increases the erosion along the coast. As a result, Arctic coastal retreat has increased more than two times in the last few decades (B. M. Jones et al., 2008a; B. Jones et al., 2018b; Günther et al., 2015; Irrgang et al., 2018; B. M. Jones et al., 2020). Observations along the various Arctic coasts have led to the establishment of a link between increased coastal erosion and a smaller extent of sea cover (K. Barnhart, Overeem, & Anderson, 2014; Stroeve & Notz, 2018), warmer air temperature (Serreze et al., 2008; Cohen et al., 2014) and increased permafrost temperature (Nielsen et al., 2021a).

Increased Arctic coastal erosion poses a significant threat to the communities living close to coasts and rivers. Infrastructure along the shores is compromised, heritage sites are at risk, and the lifestyle of the indigenous people is also affected (B. M. Jones et al., 2008b). Moreover, within the next decade, it is expected that the surface air temperature will exceed the normal range of variability. In contrast, in the case of Arctic sea ice, the natural range of variability is already observed to be exceeded (Landrum & Holland, 2020). A pan-Arctic model by Nielsen et al. (2021b) predicts that Arctic coastal erosion will exceed the natural variability range before the end of the century, with a 66% probability of exceeding by 2023 and a more than 90% probability of exceeding before 2049.

The understanding of the governing mechanisms of Arctic coastal erosion is still limited. The fundamental element of Arctic coastal erosion, the presence of permafrost, creates a different condition compared to coastal erosion in a warmer climate. Permafrost acts as a nonerodible structure when no thermal source is present. Along with the thermal drivers, the mechanical component also contributes to erosion. Coastal erosion in the Arctic is sensitive to the presence of sea ice, which has a damping effect on the waves propagating towards the coast (Squire et al., 2009).

Are F (1988) described two mechanisms that govern coastal erosion in the Arctic: thermodenudation and thermoabrasion. In the thermodenudation process, thermal energy melts the permafrost during the summer, leading to slumping of the thawed bluffs by gravitational forces. The slumped materials are removed from the beach by waves, tides and storm surges. Thermodenudation is a continuous process and contributes to the slow retreat of the coast. In contrast, thermoabrasion is rapid and episodic. Thermoabrasion is triggered during summer storms when surges cause inundation of the beach. This leads to the formation of the wave-cut niche at the base of the bluff. The growing niche becomes deep enough to trigger bluff collapse at one point. The collapsed bluff degrades on the beach and eventually washes away under hydrodynamic forcing.

Several models have been developed to simulate Arctic coastal erosion during the past decade. Most of these models focus on bluff failure, where the growth of the niche is the central factor of the erosion mechanism. Such process-based models simulate wave-cut niche growth at the bluff base, destabilise the overhanging portion and lead to bluff failure. The earlier work of Kobayashi (1985) acts as the basis for most of these models. Kobayashi (1985) developed an analytical solution of the inward growth rate of the niche as a function of the temperature of the incoming seawater, the depth of the water at the base of the bluff and the duration of the inundation. Additionally, niche models developed for melting of icebergs via waves and currents (Russell-Head, 1980; White et al., 1980) have also been used with modifications (Bull et al., 2020). Hoque and Pollard (2009) modelled bluff failure as a loss of balance (moment failure) and shear failure (mechanical strength). A process-based model to connect niche growth and bluff collapse with hydrodynamic forcing was introduced by Ravens et al. (2012). They included oceanographic boundary conditions using 12-hour time steps. Ravens et al. (2012) coupled four physical processes as modules: storm surge, niche growth, collapse of the overhanging bluff over the niche and degradation of the collapsed bluff. Barnhart et al. (2014) expanded the model of Ravens et al. (2012) and incorporated the stability concept of Hoque and Pollard (2008). Barnhart et al. (2014) also used smaller time steps (3 h) to capture erosion at higher temporal resolutions. To include the effect of morphological changes such as changes in the coastal profiles of the Arctic coasts, Ravens et al. (2017) used the open-source software package XBeach (Deltares, 2022) to simulate wave propagation, sediment transport and slumping. The latter was achieved by modifying the avalanching module in XBeach originally developed for sandy dunes. Bull et al. (2020) introduced finite element analysis to understand niche-induced bluff collapse in detail. Frederick et al. (2021) developed the finite element model to obtain a detailed analysis of the formation of the niche and subsequent bluff collapse without assuming any predetermined failure planes. Rolph et al. (2021) developed a pan-Arctic level erosion model based on the thermal energy balance on the beach, a model originally proposed by Kobayashi et al. (1999).

Arctic coastal erosion is a combination of various physical processes. While detailed models of some of the processes exist, for example, the formation of a wave-cut niche during a storm (Kobayashi, 1985; Frederick et al., 2021), a long-term generic (not site-specific) comprehensive model has yet to be achieved (Irrgang et al., 2022). The process-based numerical models developed for various sites usually simplify physics. More importantly, the interactions between the processes in the models are either ignored or made one-way (the processes are consequential, following a strict order of precedence). The existing models are not generic to all Arctic coasts, specifically for beaches where erosion is a mix of thermodenudation (dominated by thermal processes) and thermoabrasion (mainly mechanically driven).

This paper describes a comprehensive model that couples the thermodenudation and thermoabrasion processes with the morphodynamics of coastal profiles. The waves and related hydrodynamic forcing are simulated using XBeach. The other dominant processes related to erosion are simulated by the in-house developed modules. We adopt a modular approach for the numerical implementation where the submodules communicate with each other at three-hour intervals. The model is calibrated with field measurements from one of the Arctic coasts along Russia's Kara Sea. The field measurements were conducted at Bayadaratskya Bay in the Kara Sea during summer from 2012 to 2019. The soil temperatures inside the coastal bluffs were continuously monitored by placing thermal strings inside boreholes. The simulation by our model shows close agreement with the field measurements.

2 Model Description

A typical Arctic coast consists of a permafrost bluff at the end of a narrow beach. The base of the bluff is usually slightly above the highest astronomical tide and thus unreachable by seawater except during extreme events such as storms in the summer; see Figure 1. During winter, the beach is generally covered with snow, and the sea is covered with ice, which prevents waves from reaching the coast. When sea ice disappears in the summer, waves generated in the deep sea can propagate all the way to shore. Wave run-ups on an ordinary calm summer day rarely reach the bluff's base. Surges caused by storms during the summer can raise the water level enough to reach the bluff. The warm seawater creates a niche at the bluff base. When the depth of the niche is deep enough, the overhanging part of the bluff may collapse. During winter, the erosion is primarily inactive. However, it is observed that even when the waves are practically nonexistent due to sea ice, some part of the bluff face may be exposed to warmer air in the early summer, which is susceptible to thawing. The Arctic coast-related terminologies used in this paper are defined in detail in Appendix:A2.

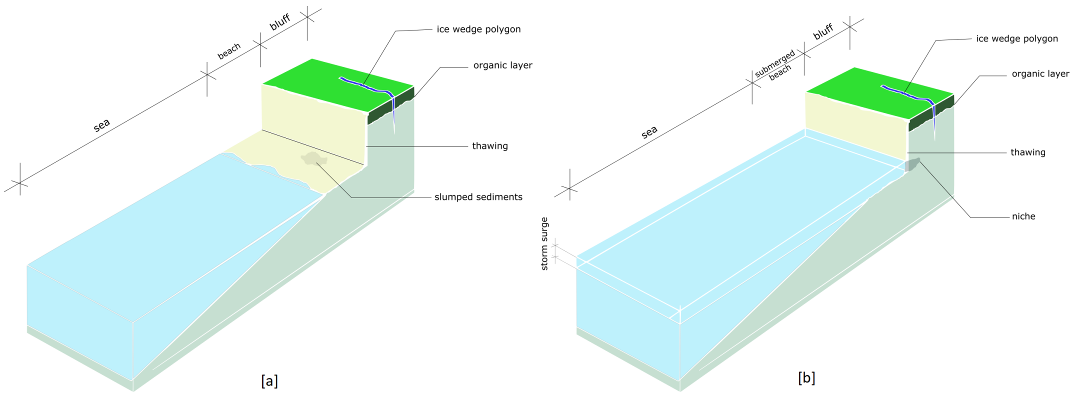

Figure 1: a) A typical Arctic coast during summer. Usually, the Arctic beaches are narrow and permafrost-rich bluff stands at the end of the beach. b) During an extreme event, storm surge pushes the water to reach the base of the bluffs, and a wave-cut niche develops at the base.

2.1 Problem formulation

The dynamics of erosion at Arctic beaches start with offshore wave generation. Waves, tides and returning currents act as the mechanical driving force in a similar way the forces act on the sandy beaches (Are & Reimnitz, 2008). The thermal driving forces are the warm seawater and air that bring thermal energy to thaw the permafrost. The physical processes involved in Arctic coastal erosion can be grouped according to both temporal and spatial scales; see Figure:2. For the former, the processes can be grouped under the periods of summer, winter and extreme events. The extreme events are the storms during the summer, typically when the wind speed exceeds 10 m/s, sustained over a period of at least 12 hours, and the dominant wind direction is normal to the shoreline, i.e., $\pm 60°$(Atkinson, 2005). The processes can be also grouped under offshore, nearshore, and bluffs on the spatial scale.

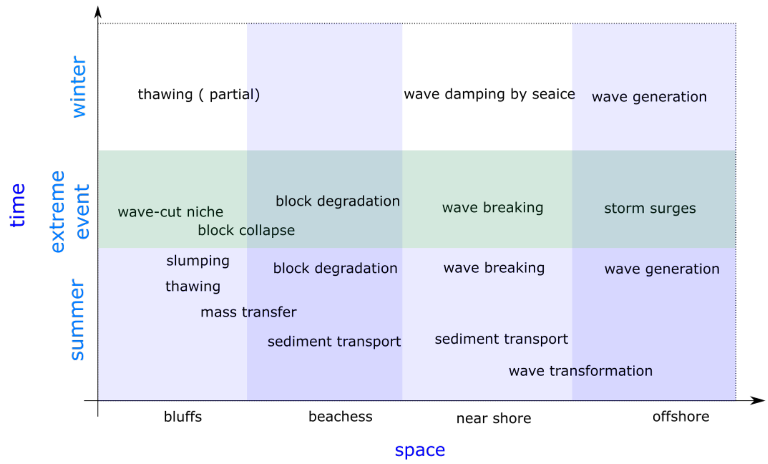

Figure 2: The processes of Arctic coastal erosion in time and space are shown. The temporal divisions are winter, summer and extreme events, and the spatial zones are offshore, nearshore and bluffs.

2.1.1 Temporal domain

Winter

Winter is defined herein as the period of time where the average air temperature over seven consecutive days remains below zero degrees. During winter, the sea is covered with ice, and hence, no hydrodynamic forcing is active on the beach or the bluff face. The ambient air temperature remains below zero, and snow covers the beaches. Near the end of the winter, erosion activities such as thawing of the exposed bluffs and slumping of the thawed materials may be observed when snow melts and bluffs are exposed to the warmer air.

Extreme events

Extreme events during summer contribute to episodic and sudden erosion by thermoabrasion, one of the two prominent erosion mechanisms in the Arctic. In these dynamics, the surge created during the storm inundates the beach in front of the bluff. The warm seawater touches the bluff and creates a niche at the base of the bluff. It may take a few storms for the niche to grow to a crtitical extent when the overhanging part of the bluff falls. The collapsed bluffs then degrade under the influence of waves. The sediments are mainly carried away offshore (as suspended sediment transport).

Summer

We define summer as the time period when the seven days of consecutive air temperature remain above zero degrees. Thermodenudation, another mechanism of Arctic coastal erosion, is observed during summer. The permafrost starts to thaw due to the warm air and seawater. The thawed material contributes little to the beach's development in most cases (#cite). The fine sediments are removed from the beach by hydrodynamic forcing, such as high tides, wave run-ups, and storm surges.

2.1.2 Spatial domain

Offshore

Offshore is defined herein as the zone of deep waters where water depth (h) is greater than peak wavelength (λ) divided by 20, i.e., $h > \lambda/20$. Waves generated offshore propagate to the shore during the summer when the ice concentration at sea is low (e.g., below 15%). During the summer, the storms push the water against the coast, and the water level rises, a prerequisite condition for thermoabrasion. The sea ice extension shrinks during the summer, leading to large waves and significant storm surges. It is reported that along the Beaufort Sea, the surges can be as high as 1.5 metres to 2 metres (Ravens et al., 2012; K. R. Barnhart et al., 2014). Along the Kara Sea, the surges are close to 0.7-1 metres (Isaev et al., 2019).

Near shore

Nearshore is defined herein as the area with intermediate and shallow waters where $h < \lambda/20$. The wave generated in the offshore zone is transformed after entering the nearshore. The sediment transport is also stronger at the near shore.

Bluffs

The bluffs are defined as the part of the coastal profile from the shoreline until a considerable distance within bluffs (for our model, we considered 35 metres from the base of the bluffs in the onshore directions). This part is considered the 'dry' portion of the profile regarding convective heat transfer. Continuous thawing occurs at the bluff face during the summer. Thawed sediments fall down the base of bluffs under the force of gravity. The wave-cut niche, bluff collapse and bluff degradation are also observed during storms. The mass loss of the bluffs generates a sediment flux that influences the morphological changes in the nearshore.

2.2 Process-based model of erosion

In this study, we present a comprehensive process-based model that can simulate long-term coastal erosion in the Arctic with high fidelity. The model includes the physical processes that govern coastal erosion in a domain ranging from offshore to the bluff. Figure 3 explains the physical processes included in the model in the time and space domains. Table 1 shows the input parameters used in the model.

Table 1: The list of main parameters used to describe the models.

parameter	definition	typical value	units	references
thermal properties				
h_a	convective heat transfer coefficient of air	100	$W/m^2 - k$	(Kobayashi et al., 1999)
h_w	convective heat transfer coefficient of water	700	$W/m^2 - k$	(Kobayashi et al., 1999)
L_t	latent heat of permafrost	1.6×10^7	kg/m^3	(Kobayashi et al., 1999)
T_a	Temperature of air	varied	°C	NOAA
T_w	Temperature of water	varied	°C	NOAA, sea surface temp
T_s	Temperature of soil	varied	°C	field measurements
geometry				
x_t	thawing depth	varied	m	
h_{id}	water depth at the base	varied	m	
h_m	mean water depth	varied	m	
h_t	tide compared with MSL	varied	m	
β	niche opening parameter	2	-	Kobayashi (1985)
η	storm surge level compared with MSL	-	m	Eq.1
m_{cr}	critical slope of slumping	0.1-1	-	field observations
T_{HF}	distance from niche to the ice-wedge polygon	5-14 metre	m	field observations
U_w	wind speed	-	m/s	NOAA reanalysis
time steps				
dt_x	timestep within Xbeach	varied	s	XBeach Manual
dt	timestep within modules/ global timestep	10800	s	based on 3 hour sea state
dt_m	timestep between two field measurements	365	days	Field report

Each spatial zone is considered a module that is separated by the boundaries BC1 to BC4. We grouped the processes involved in erosion under the three modules: offshore, nearshore and bluffs. Each process active in the module is termed a submodule. The modules and boundaries are shown in Figure 3. The spatial domain begins at BC1, which is the offshore edge of the ice extension. BC2 is the nearshore outer boundary where $h/\lambda \leq 0.5$. The BC3 boundary stands at the swash zone.

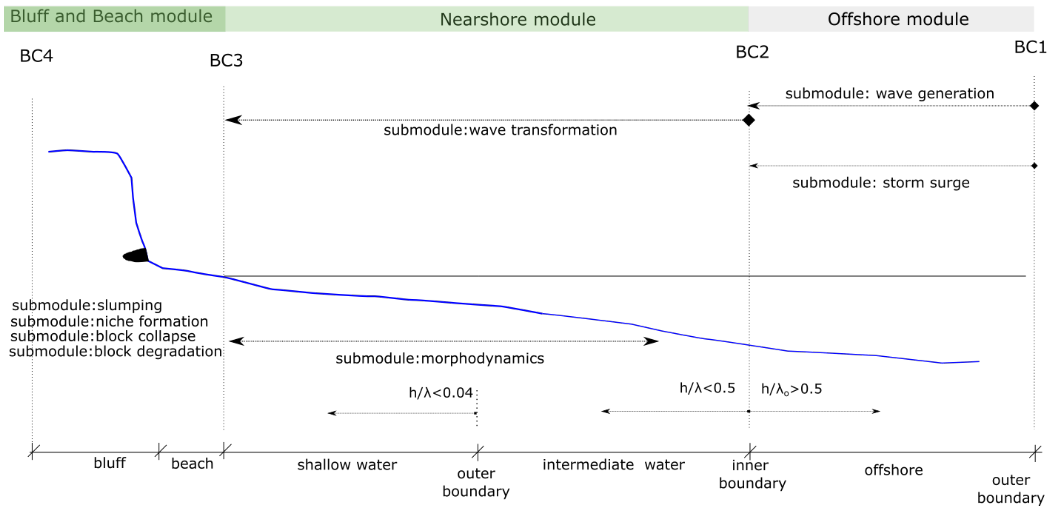

Figure 3: Three distinct modules are defined using the boundary conditions (BC).

2.3 Offshore module

The offshore module simulates the wave generation and transformation of waves in the deeper waters from BC1 to BC2. The module consists of two submodules: (1) storm surge and (2) wave generation.

2.3.1 Submodule: Storm surge

The storm surge submodule is a one-dimensional (1D) storm surge model used to calculate the surge as a function of wind speed, alongshore current and the Coriolis effect. The submodule estimates the storm surge (η) relative to the mean sea level (MSL). The storm surge submodule is the steady-state solution of the following equation (Dean & Dalrymple, 1991):

$$g\left(h_m + \eta\right)\frac{\partial \eta}{\partial x} = \left(h_m + \eta\right) fV + \frac{\tau_{sx}}{\rho} \tag{1}$$

where g is the gravitational acceleration, h_m is the mean water depth (time averaged), $f = 2sin\omega$ is the Coriolis frequency of Earth, ω is the latitude of the study area (in radians), ρ is the seawater density, V= depth-averaged alongshore water velocity, $\tau_{sx} = \rho C_D U_w^2$ is the stress from the wind on the surface of the water, C_D is the drag coefficient ($= 2 \times 10^{-6}$), and U_w is the wind speed at 10 metres.

2.3.2 Submodule: Wave generation

Waves are generated when the sea is free of ice, i.e., during the open water season. The wave generation is simulated herein using SWAN (SWAN, 2021). SWAN simulates the generation and propagation of waves by assuming energy conservation by the action balance equation (Eq.2). The transfer of energy from the wind to the waves is simulated using the models of Phillips (1957) and Miles (1957). Hoque et al. (2020) showed that modelling waves using SWAN on the Arctic coast of Beaufort are in good agreement with observed data with respect to the significant wave heights and peak period.

$$\frac{\partial N}{\partial t} + \frac{\partial c_x N}{\partial x} + \frac{\partial c_y N}{\partial y} + \frac{\partial c_\sigma N}{\partial \sigma} + \frac{\partial c_\theta N}{\partial \theta} = \frac{S_{\text{tot}}}{\sigma} \tag{2}$$

where N is the action density, x, y and z are the Cartesian coordinates, $c_x = c_{g,x}+U_{wx}$ and $c_y = c_{g,y}+U_{wy}$, c_g is the group velocity of the wave, U_w is the wind velocity at 10 metres, σ is the frequency, θ is the angle, and S_{tot} is the total sink or source. For details, we refer to the SWAN manual (Booij et al., 2000).

2.4 Nearshore module

The module simulates wave transformation and morphological changes due to sediment transport and hydrodynamic forcing. The module boundaries are in the intermediate to shallow waters, from BC2 until BC3 of Figure:3. In our model, we used XBeach to simulate the hydrodynamics of the nearshore. XBeach is an open-source numerical model developed to simulate morphological changes on the scale of one to ten kilometres and the time scale of a storm (several days). The submodules under the nearshore module are (1) morphodynamics and (2) wave transformations.

2.4.1 Submodule: Morphodynamics

The morphodynamic submodule simulates sediment transport and the changes in the sea bed. Sediment transport is estimated by using the depth integrated model proposed by (Galappatti, 1983), a feature built into the XBeach. The governing equation stands as:

$$\frac{\partial hC}{\partial t} + \frac{\partial hCu^E}{\partial x} + \frac{\partial hCv^E}{\partial y} + \frac{\partial}{\partial x}\left[D_h h \frac{\partial C}{\partial x}\right] + \frac{\partial}{\partial y}\left[D_h h \frac{\partial C}{\partial y}\right] = \frac{hC_{eq} - hC}{T_s} \tag{3}$$

where C represents the depth-averaged sediment concentration, D_h is the diffusion coefficient of diffusion,T_s is a function of water depth, h and sediment fall velocity, w_s, C_{eq} is the equivalent sediment concentration, and u, v are the particle velocities in the x (offshore) and z (vertical) direction.

The bed update within XBeach due to the sediment flux is achieved by using the following continuity equation:

$$\frac{\partial z_b}{\partial t} + \frac{f_{mor}}{1-p}[\frac{\partial q_x}{x} + \frac{\partial q_y}{y}] = 0 \tag{4}$$

where q_x and q_y are the sediment flux in the x and y directions, z_b is the coastal profile, f_{mor} is a morphological factor (we used 1 in the module) and p is the porosity. For details, we refer to the XBeach manual available at *xbeach.readthedocs.io*.

2.4.2 Submodule: Wave transformation

XBeach is used to simulate the wave transformation from the BC2 boundary, where $h \leq \lambda/2$. XBeach includes the hydrodynamic processes of short wave transformation (refraction, shoaling and breaking), long wave (infra-gravity wave) transformation (generation, propagation and dissipation), wave-induced setup and inundation (Roelvink et al., 2010). XBeach requires the inputs of wave spectral parameters (e.g., significant wave height (h_{m_0}, peak frequency (f_p)) and water level (wl), among other inputs at BC2.

2.5 Bluff module

This module simulates the processes of thermodeundation and thermoabrasion within the beach and bluff. Bluffs are the most active zone regarding coastal erosion. The module consists of the submodules: 1) permafrost thaw, 2) slumping 3) niche growth 4) bluff collapse and 5) buff degradation.

2.5.1 Submodule: Permafrost thaw

We divide the permafrost thaw along the coastal profile into four sections, as shown in Figure 4. The warmer air and seawater bring the thermal energy necessary to thaw the permafrost inside the bluffs. The sections are defined based on the nature of the convective heat transfer. The four sections are the bluff surface, bluff face, beach and seabed (definitions are in appendix:A2).

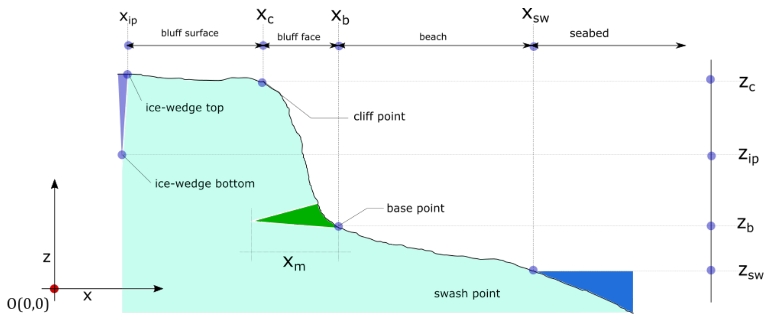

Figure 4: The coastal profile can be divided into four sections based on the thermal energy transfer mechanism. The most active portion in terms of thawing is the bluff face.

The thawing depth (x_t) is defined as the depth of permafrost melting or freezing face from the coastal profile, normal to each point, as shown in Figure:5. Stefan's equation can be used to determine the thawing depth (x_t) (Guégan, 2015):

$$x_t = \sqrt{\frac{2k_u T_0 t}{L}} \tag{5}$$

where t is the length of time (days), L is the latent heat of fusion, and $k_u = 1.6Jm^{-1}s^{-1}K^{-1}$ and T_0 are the temperatures of the bluffs. However, Eq.5 overestimates the thawing and freezing depth (Guégan, 2015). The equation does not consider the fluid and surface interactions, air/water velocities, turbulence and geometric orientations. Eq.5 is not suitable for our model since we want to treat the dry and wet (submerged) parts of the coastal profile separately. We adopted another approach to estimate the thawing depth by calculating the heat transfer and subsequent thawing and freezing (Ravens et al., 2017). The energy transfer from the seawater or air to the sediment is estimated from the convective heat transfer equation:

$$Q_{w/a} = h_c(T_{w/a} - T_s) \tag{6}$$

where $Q_{w/a}$ is the thermal energy transfer from water or air to the bluffs ($Jm^{-2}s^{-1}$), h_c is the convective heat transfer coefficient; different for air and water, $T_{w/a}$ is the temperature of the water or air, and T_s is the temperature of the seabed and bluff.

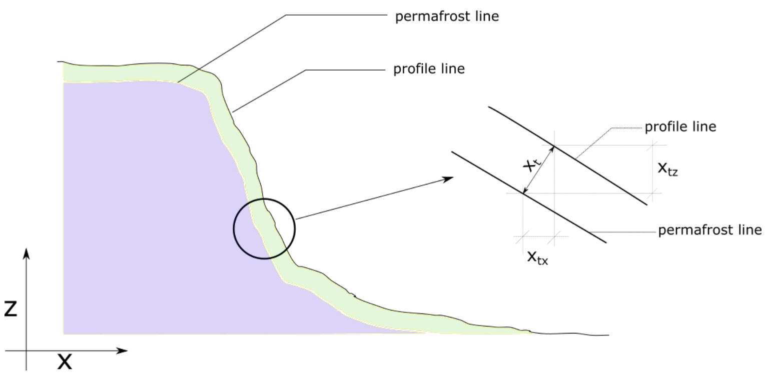

Figure 5: The thawing depth is the distance normal to the permafrost to the surface of the bluffs (x_t).

Eq.6 then can be used to determine the thawing depth by using Eq.7:

$$\frac{x_t}{dt} = \frac{Q_{w/a}dt}{\rho L_t} \tag{7}$$

where L_t is the latent heat of permafrost, taken as $L_t = 1.6{\times}10^7 J/m^3$, dt is the time duration in seconds and x_t is the thawing depth assumed to be normal to the surface (see Figure:5).

The benefits of using Eq.7 over Eq.5 in our model are (1) the convective heat transfer coefficient can be calibrated to represent the different heat fluxes at bluff-surface, bluff-face, beach and seabed and (2) the equation is also valid for freezing when the fluid temperature goes below zero, allowing the submodule to be active for all the seasons.

2.5.2 Submodule: Slumping

The thawed sediments at the bluff face fall due to gravitational forces since the slope of the bluff faces is quite steep. The limiting parameter controlling the mass fluxes caused by slumping is the thawing rate (dx_t/dt). However, the slumping process is triggered by the slope of the bluff face. A critical slope on the bluff face, m_{cr} is defined at which the thawed material will fall under the influence of gravity (see Figure:6). The following conditions must be fulfilled to trigger slumping.

$$\frac{dz}{dx} \geq \begin{cases} m_{cr;w} & \text{if } x_t > 0, h > 0.05m \\ m_{cr;a} & \text{if } x_t > 0, h < 0.05m \end{cases} \tag{8}$$

where dz/dx is the slope of the coastal profile at a given point, $m_{cr;a}$ and $m_{cr;w}$ are the critical slopes for dry and wet conditions, respectively, and h is the water depth at the grid point. When the water depth reached $h \geq 0.05m$, we considered the grid to be submerged, and x_t is the thawing depth. The process of slumping of the thawed layer is discussed in detail in appendix:A32.

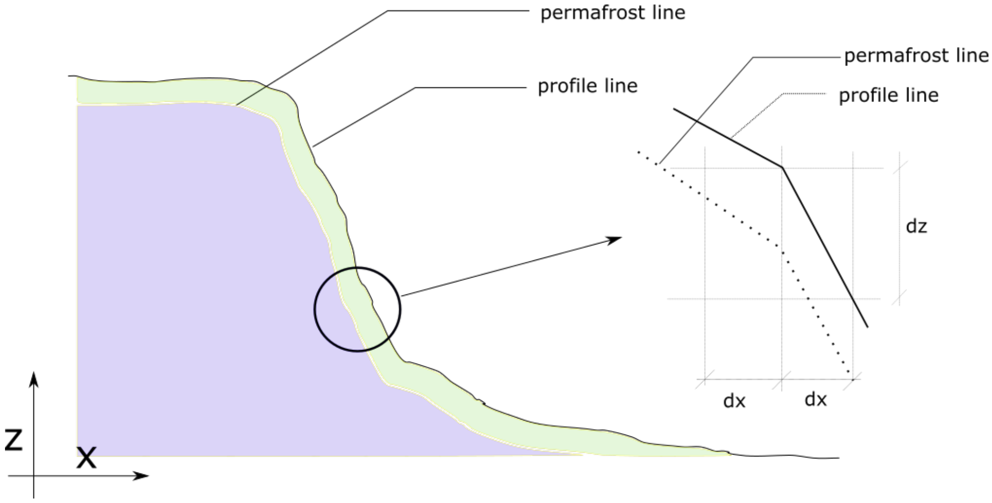

Figure 6: Slumping occurs when the thawed materials fall due to gravity. The condition of the triggering is: (1) thawing depth (x_t) is greater than zero and (2) slope at the point (dz/dx) is greater than the critical slope (m_{cr}).

2.5.3 Submodule: Niche growth

When the water level reaches the base of the bluff (point B in Figure 7), the warm water creates a niche. The geometry depicted in Figure 7 is adopted and simplified from the Kobayashi (1985) model.

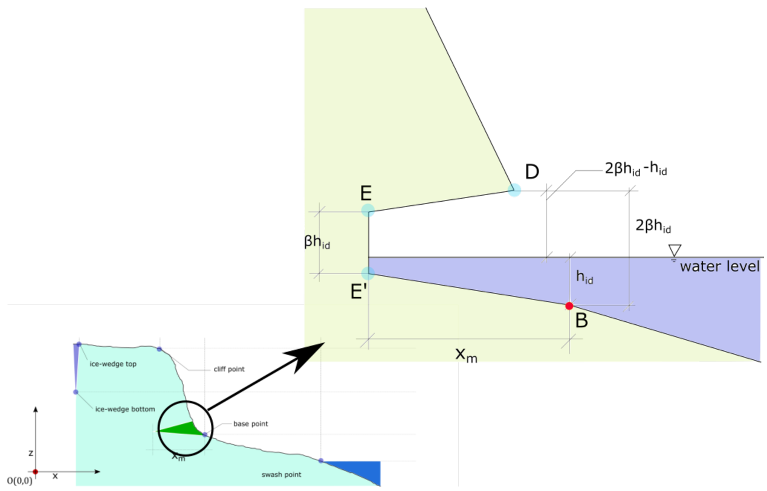

Figure 7: Niche geometry during the storm surge; simplified from Kobayashi (1985).

The melting face, line EE', is vertical and assumed to be βh_{id}, where β is the empirical parameter and h_{id} is the water depth at the base of the bluff. The value of β is taken as 2(Ravens et al., 2012). The niche depth, line BE'=x_m, is estimated from the equation:

$$x_m = 2\zeta_m\sqrt{\epsilon t} \tag{9}$$

where h_{id} is the time-averaged depth of water at the base of the bluff, g is the gravitational acceleration, ϵ is the surf zone diffusivity $\epsilon = Ah_{id}\sqrt{gh_{id}}$, A is an empirical constant, taken as 0.4 (Longuet-Higgins, 1970), $\zeta_m = 0.0094(T_a - T_m)$, T_a is the temperature of the seawater and T_m is the salinity adjusted melting point of the ice.

2.5.4 Submodule: Bluff stability

The wave-cut niche at the base of the bluff creates instability, which may lead to the collapse of the bluffs. A critical combination of the various geometric parameters, such as niche opening, niche depth, the position of ice-wedge polygon and mechanical strength parameters, such as internal friction and cohesive strength, leads to the collapse of the bluffs. The location of the failure line and plane may vary depending on the combinations of the various parameters. Two principal modes are identified for bluff collapse: (1) shear failure and (2) overturning failure (Hoque & Pollard, 2008). Shear failures are related to the mechanical strength of the bluffs. In Figure:8a, one such failure is depicted. The shaded region over the niche is susceptible to collapse. The failure line in this case is GE, and the shaded region by the geometry GCDE is collapsed. A generalised and simplified condition of shear failure of the bluff is Eq:10 (Hoque & Pollard, 2009):

$$c \cdot T_{ib} + W cos\alpha \cdot tan\phi < W sin\alpha \tag{10}$$

where α is the angle of inclination of the failure plane, ϕ is the angle of internal friction of the bluffs, T_{ib} is the tensile failure line of the bluff, c is the tensile strength of the bluff, and W is the weight of the collapsed bluff (weight of the GCDE portion in the Figure:8a).

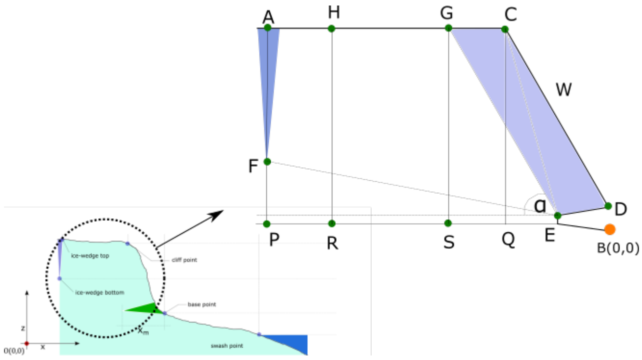

(a) Shear failure of the bluffs, described by Eq.10.

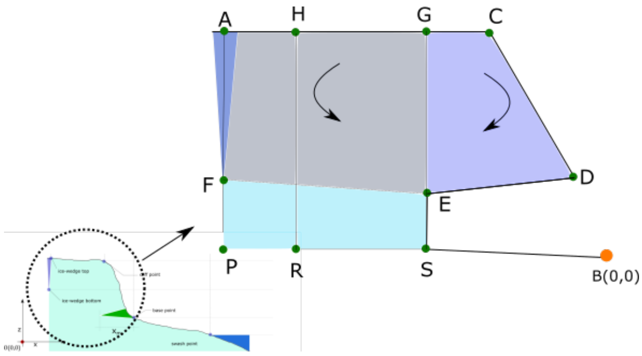

(b) Overturning failure of the bluff, described by Eq.11.

Figure 8: Two common failure modes of bluff collapse.

In the overturning failure mode, the failure is initiated by the moment created by the overhanging portion of the bluff. The overturning occurs at the melting phase of the niche at point E in Figure:8b. The shaded overhanging portion (GCDE) creates the driving moment in favour of collapse, which is countered by the moment created by the remaining portion of the bluff (AHGEF). A small contribution comes from the friction along failure line EF and line AF. The failure mode is generalised by the following equation (simplified from the models by Hoque and Pollard (2009) and K. Barnhart, Anderson, et al. (2014)):

$$\tau_d > \tau_r + c_p T_{HF} + c_{ice} T_{VF} \tag{11}$$

where τ_d is the moment created by the overhanging bluff at the turning point, τ_r is the opposite moment created by the rest of the bluff, c is the cohesive strength of the bluff (different for ice and permafrost), T_{HF} is the horizontal failure line (line FE in the Figure:8b), and T_{VF} is the vertical failure (line AF).

2.5.5 Submodule: Degradation of collapsed bluffs

When a bluff collapses due to niche formation, it stays on the beach. The convective heat transfer from water and air melts the ice within the pores. The degradation rate of the bluff can be estimated from the following equation (Ravens et al., 2012):

$$
\begin{aligned}
ER &= aH^n(T_w - T_m) \\
M_i &= M_{i-1}(1 - ER)
\end{aligned}
\tag{12}
$$

where M_i is the mass of the collapsed bluff at the end of timestep i, M_{i-1} is the mass of the bluff at the end of the previous timestep $i-1$, T_w is the temperature of the seawater, T_m is the salinity adjusted melting point of ice, H is the significant wave height at the 3 metre water depth, and a and n are the empirical parameters. Ravens et al. (2012) estimated that the values of a and n are $800kg/m - {}^\circ C$ and 1.47, respectively.

2.6 Numerical implementation

2.6.1 Simulation of the nearshore module by XBeach

We choose XBeach to simulate the nearshore module (from BC2 in Figure:3) until bluffs. The wave transformation and morphodynamic submodules are included inside XBeach. The users can turn them on and off for a particular time step. We couple the other submodules with XBeach. The timestep for the model is chosen to be 3 hours (Figure:9). We simulate the nearshore modules with XBeach for the i-th timestep and analyse the results. We determine the bed level changes, the average water depth at the base of the bluffs (h_{id}), and the average water depth at each grid (to determine the wet/dry condition for convective heat transfer). The output of XBeach is then fed into the submodules of slumping, thawing depth, niche growth, and bluff stability.

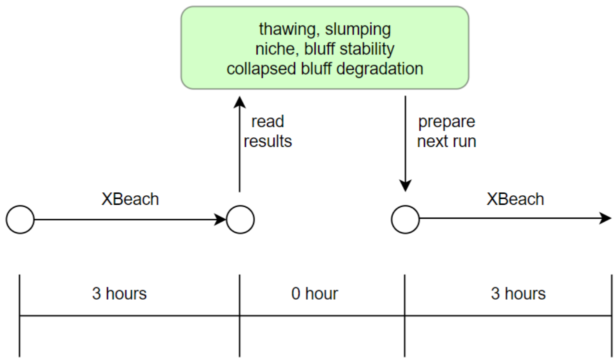

Figure 9: XBeach simulates the nearshore module. The output of the XBeach is analysed and used as inputs for other submodules.

2.6.2 Modelling permafrost and thawing depth

XBeach was not originally developed to simulate permafrost or thawing. The permafrost and the thawed layer above the permafrost need to be treated separately to simulate thermodenudation. The thawing submodule calculates the thawing depth at the interval of each time step. The thawed layer above the permafrost reacts to hydrodynamic forcing similar to a typical coastal profile in a tropical or subtropical climate. Therefore, the morphodynamic submodule is applicable for the thawed layer but not for the permafrost layer. Within XBeach, there is a feature of a nonerodible surface layer. The 'nonerodible surface' aims to treat the effect of hard structure on the morphological changes in the coastal profile. The developers of XBeach introduce the concept of a nonerodible surface to allow users to include a surface that is not affected by hydrodynamic forcing. No sediment transport is permitted even if this surface is exposed. The nonerodible surface can be defined with $'ne\_layer'$, and the user can place it inside the dune, beach and seabed. The permafrost acts similarly to a nonerodible surface, only that the permafrost line is a moving boundary with respect to time. In the numerical model, we achieve it by updating the $'ne\_layer'$ of XBeach from the thawing depth (x_t) estimated at the end of the time step.

2.6.3 The workflow of the numerical model

As discussed earlier, the morphological changes and wave transformations are simulated by XBeach. The other submodules are coupled with the XBeach. The workflow of the submodules is shown in Figure:10. At the inception of the simulation, global parameters such as the latent heat of permafrost melting (L), the tensile strength of bluffs (τ), geometric parameters such as β and $m_c r$ for air and water, etc., are loaded. These parameters are time independent, i.e., remain the same for all timesteps. The input parameters, such as air temperature (T_a), water temperature (T_w), ice concentration (i_{con}), wind speed (U_w), bluff temperature (T_s), and tide (η_{tide}) are dependent on time. The model requires the time series of these input parameters at the same time interval as the global timestep. We set the global timestep as 3 hours to be consistent with the three-hour sea-state and wave spectrum.

At the beginning of the i-th iteration, we must check if the current timestep is within the simulation duration. If the condition is satisfied, we load the input parameters from the respective time series for the i-th timestep. The numerical model checks the ice concentration (i_{con}) for the current time step. From here, it is possible to proceed following two different routes. The offshore and nearshore modules are activated if the ice concentration is less than 20%. If the ice concentration is more than 20%, then the numerical model skips the offshore and nearshore modules. An ice concentration of more than 20% indicates no activity in offshore and nearshore modules. However, thawing and slumping might still occur even without hydrodynamic forcing. The numerical model activates the slumping submodule within the bluff module to accommodate this condition. The slumped sediments are moved to the bluff base. Since no hydrodynamic forcing is present in this route, the deposits at the base will not be transferred, and the model allows the accumulation of slumped sediments over the time steps. The accumulated sediments will be transported later when the nearshore module is activated.

Another route in the workflow is triggered when the ice concentration is less than 20%. If this condition is satisfied, the offshore and nearshore modules are activated. The submodules of the offshore, wave generation and storm surge are turned on. The outputs of the wave generation and storm surge submodules are the storm surge water level (η) and wave spectrum at boundary BC2. The boundary conditions at BC2 are thus dependent on the offshore module. The outputs of the offshore module are fed into the submodules of the nearshore module, i.e., the wave transformation and morphology submodules. The water level is updated at BC2 for the tide and storm surge.

The nearshore module simulates the sediment transport, currents, water level setup, and morphological changes due to hydrodynamic forcing. The outputs of the nearshore module are used as input parameters for the submodules of the bluff module. If the water level at the base of the bluff (h_{id}) is more than 10 cm, then the niche submodule is activated. We also calculate the time-averaged water depth at every grid point to determine whether the coastal profile is wet or dry at the i-th time step. The dry and wet grid points of the coastal profile are treated differently with respect to convective heat transfer and slumping (Eq.7).

The model enters the bluff module, and if the h_{id} is less than 10 cm (which means the sea is calm, it is a no storm condition), the slumping submodule is turned on. If h_{id} is greater than 10 cm, the niche submodule is activated, and it calculates the growth of

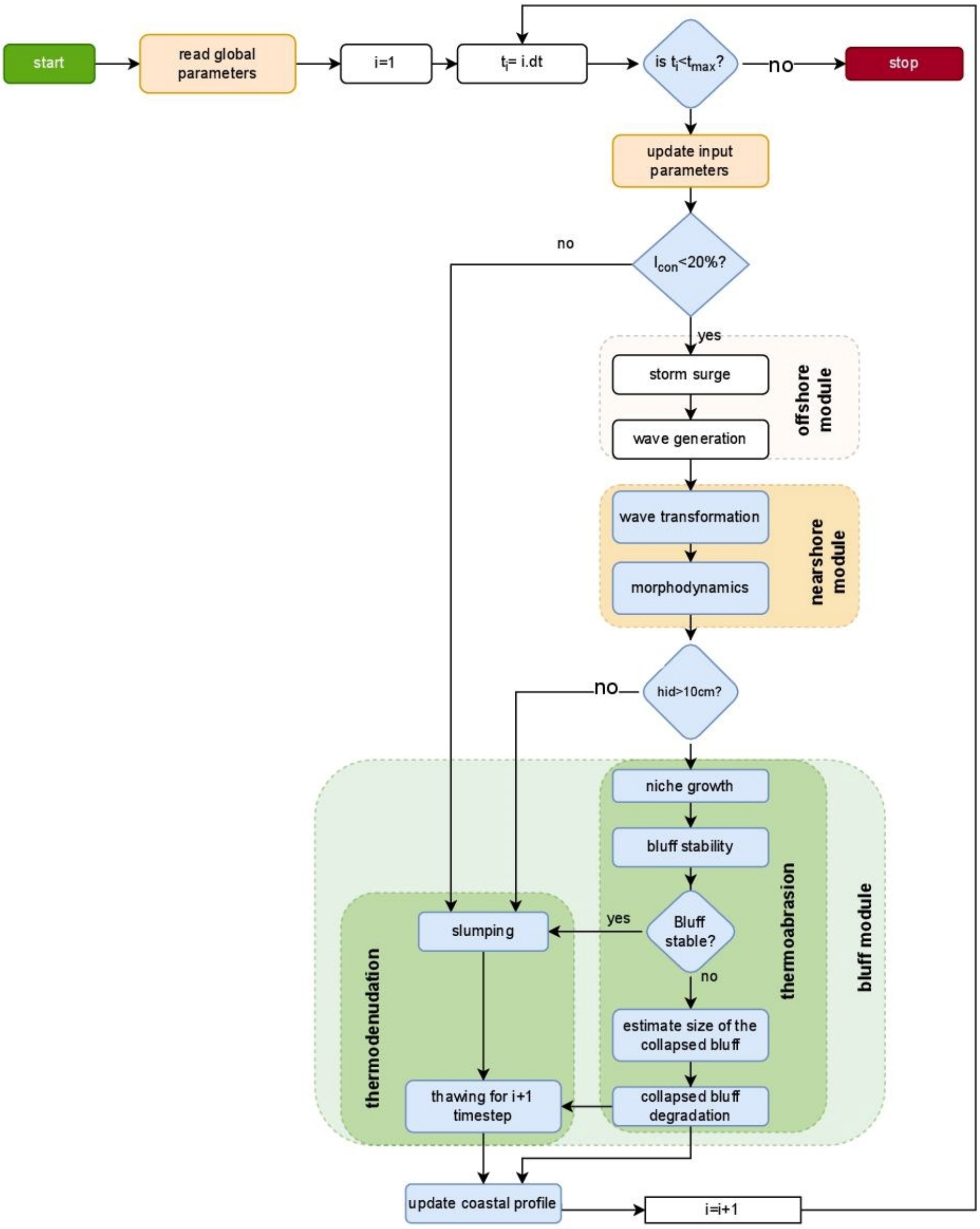

Figure 10: Workflow of the numerical implementation of the submodules.

the niche. The niche geometry is fed into the bluff stability submodule to check whether a collapse is triggered. The model turns on the thawing depth submodule when no bluff failure is recorded. When the model registers a bluff failure, the model estimates the collapsed bluff's size, and the collapsed bluff degradation module is activated. After that, we calculate the thawing depth at each grid point for the i+1 th time step. The last step of the model run at the i-th time step is to register the changes and update the coastal profile to simulate the i+1 th profile.

2.7 Application of the model

The model described in this section is generic and thus applicable to most Arctic coasts for all seasons. Both thermodenudation and thermoabrasion can be simulated simultaneously. In the upcoming sections, we demonstrate in detail the application of the numerical model. The model is first calibrated using field measurements from an Arctic coast. The subsequent validation using another set of field observations is performed.

3 Field Observations

Field investigations on one of the Arctic coasts, Baydaratskya Bay in the Kara Sea, have been conducted since the summer of 2012. The study area is in northeast Russia (68.853096°N; 66.891730°E). The coast is situated in the gulf between the Ural coast and the Yamal Peninsula (see Figure:11a). The region is not densely populated, the number of infrastructures is limited, and few indigenous settlements are present in the area. The harsh climate and lack of communication facilities hinder continuous access to the study area. Only during the summer (between June and September) is a portion of the coast investigated under the project Centre for Research-based Innovation (CRI): Sustainable Arctic Marine and Coastal Technology (SAMCoT) by the leadership of Lomonosov Moscow State University (MSU). The importance of studying the area increased after the gas pipeline of Nord Stream was constructed in 2011 (Ogorodov et al., 2013). The results obtained from the field observations, measurements, and in situ experiments form the basis of this study.

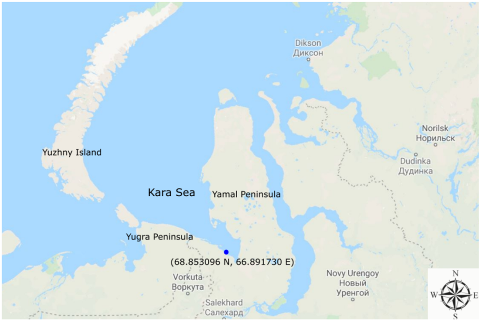

(a) The study area is situated in the Kara Sea between the shallow gulf of two peninsulas, Yugra and Yamal. Image source: Google Maps

(b) The Arctic beach is straight and consists of continuous permafrost, and the shore normal line creates a 73°line to the north. Image source: Google Maps

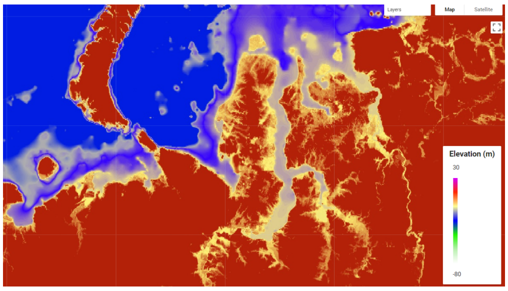

(c) Elevation map of the study area. Image source: Google Earth Engine, NOAA (Amante & Eakins, 2009)

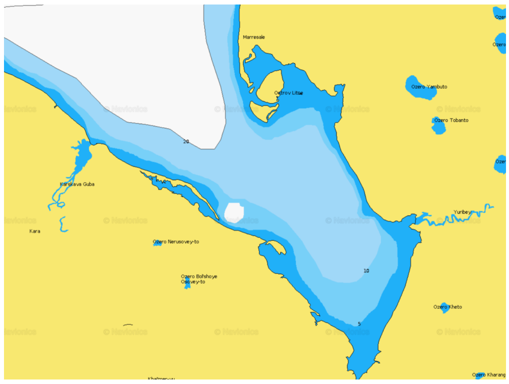

(d) In the contour map of the study area, the gulf is shallow. The water depth near the shore is less than 10 metres. image source: navionics.com

Figure 11: The study location is situated along the coast of the Kara Sea (68.853096°N, 66.891730°E). The sea is shallow, which makes it susceptible to large storm surges.

3.0.1 Morphological description

The study area can be divided into two primary observation sites, S#1 and S#2 (see Figure 12). S#1 consists of low-lying bluffs of 3-5 metres, whereas S#2 consists of 12-15 metres of high terraces. S#1 is approximately 1.2 kilometres long. The bluff surface is smoothly sloped. A leida[1] with a shoreline of 1.4 kilometres lies between the two sites of S#1 and S#2. The Leida zone has an elevation above the tide level. Only surges created by the storms in the summer can flood the leida. The surface run-off created many gullies on the surface of the area in S#1. Regarding sediment, both sites consist of silty clay, silt and silty sand. The permafrost in the study area is continuous; the annual mean

[1] a low-lying land at the coast which is flooded during summer by storm surges.

temperature at a depth of 3 metres is -4°Celsius (Isaev et al., 2019). The active organic layer is approximately 0.5-0.8 metres at the surface.

(a) The study area is divided into two distinctive sites. S#1 is closer to the Coffer dam. A small river and a leida separate the two zones. In total, eleven coastal profiles were measured during the investigations.

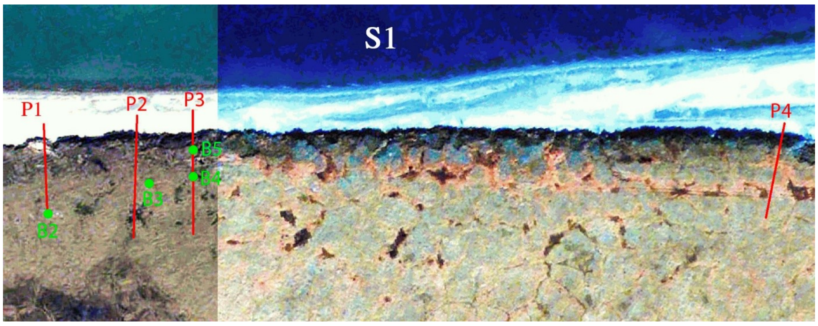

(b) Four profiles marked on the map, P#1 to P#4, are measured in Zone S#1

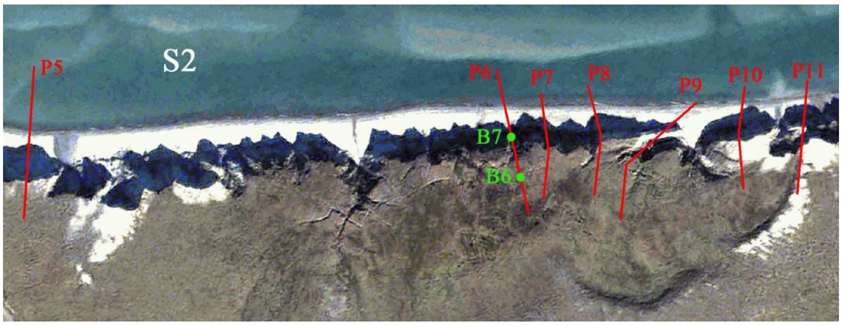

(c) The coastal profiles P#5 to P#11 are in S#2.

Figure 12: The study area consists of two sites, S#1 and S#2, with distinct bluff height differences. S#1 consists of low bluff heights. Image source: Internal reports, SAMCoT

The ice-wedge polygons are visible on the surface in S#1. Many thermokarst lakes are observed during field investigations (Figure:12b). The surface is uneven, and the organic layer is thick. Many surface run-off drainages are observed. The surface at S#2 is even, with no ice-wedge polygon visible at the surface. The vegetation is thinner, and almost no thermokarst lakes are observed (Figure:12c).

3.1 Data and Methods

3.1.1 Coastal profiles

A total number of 11 profiles are measured at different locations and different years (the positions of the profile lines are shown in Figure 12). Four coastal profiles are measured in S#1, and the rest of the profile lines are from S#2. All the profiles of the study area are surveyed using the Differential Global Positioning System (DGPS). Geo-referencing is completed using handheld DGPS receivers using some stable objects to identify the profile in the field. After that, the observations are linked to the Russian State Geodetic Coordinate System (GSK-2011). Coastal features such as bluffs and shorelines are recorded. In 2018, surveying by light detection and ranging (LiDAR) began. One profile from each site is shown in Figure 13.

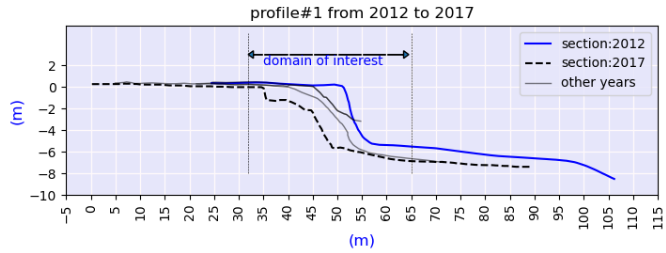

(a) Measurements of profile P#1. The profile is situated in S#1.

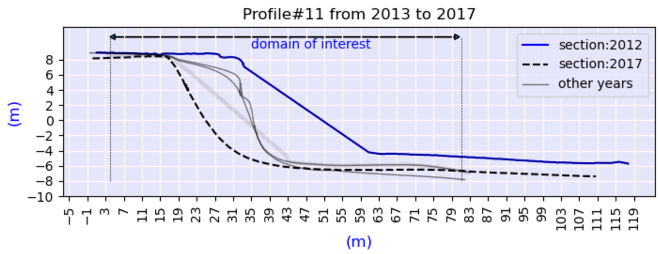

(b) Measurement of profile P#11 in zone S#2. The bluff height in this profile is approximately 14 metres.

Figure 13: Measurements of two profiles in S#1 and S#2 are shown. A borehole with a thermostring was placed in the bluff on profile P#11 to measure the soil temperature.

Profile#1 in S#1 has a bluff height of 5-6 metres. The profiles were covered with snow during measurements in 2013, 2014 and 2015. During 2017, we distinctly noticed the collapse of the bluffs near the cliff. Profile#11 from S#2 has a similar cliff retreat magnitude. Unlike Profile#1, the slope of Profile#11 remains constant over the years.

3.1.2 Nearshore marine observations

The seabed slope in the study area is 0.004 to 0.01 in the nearshore (Kamalov et al., 2006; Bogorodskii et al., 2010). The length of the open seawater season has been increasing in recent years. From 1979 to 2006, the open sea days increased by 34 days (Rodrigues, 2008). The salinity of the seawater ranges from 20-25 ppt (Stein et al., 2003). The tidal range near the shore is 70 cm, and the tidal currents do not exceed 30 cm/s (Harms & Karcher, 1999).

3.1.3 permafrost and soil temperature

As part of the investigations, boreholes are constructed at the study sites. A thermistor is used to measure the temperature at 12-hour intervals. The boreholes are approximately 3.5 to 9 metres deep. From the measurements, we observed that at the base of the bluff, the temperature of the bluff remains relatively stable and in between -5°to 0°Celsius.

3.1.4 Ambient Temperature

The air temperature of the area from 1978 to 2020 is shown in Figure:14. The data are from 1978 to 2020, reanalysis of NOAA. The mean temperature of the air (7-day mean) crosses zero degrees around week 24 (early June) and has a downwards crossing around week 40 (early October). A similar pattern is also observed for the sea-surface temperature. There is no significant lag between the air and water temperatures in the study area.

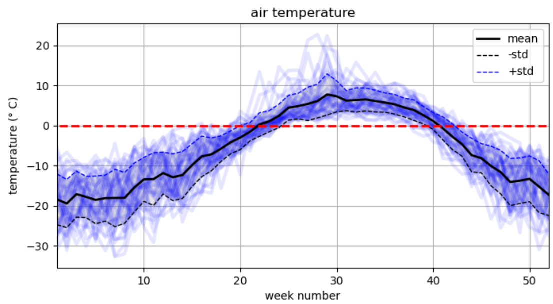

(a) Average air temperature of the study area during the year.

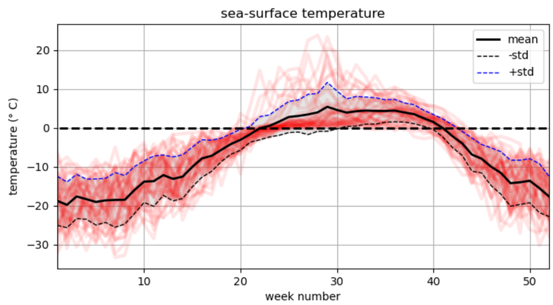

(b) the 7-day average sea-surface temperature.

Figure 14: The historic average temperature of the air and sea surface from 1978 to 2020. The mean is plotted as a thick black line along with the week number of the year. One standard deviation from the mean is drawn as a dotted line. There is almost no lag between air and sea-surface temperature. The data are from 1978 to 2020, reanalysis of NOAA.

3.1.5 Ice concentration

Ice concentration has a lag when compared with air and sea-surface temperature (Figure:15). Ice concentration declines around week 28, unlike the beginning of summer in week 24 (the upwards zero crossing of the temperature of air and water). However, the ice concentration rises after week 40 when the air and the sea-surface temperature have a downwards zero crossing. This indicates that at approximately four weeks at the beginning of the summer, thawing and slumping can occur without any significant hydrodynamic forcing in the nearshore and offshore regions.

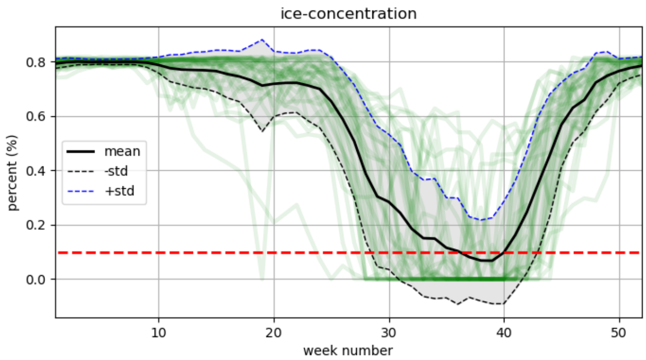

Figure 15: Average ice concentration nearshore of the study area.

3.2 Erosion pattern in the study area

We observed that both thermoabrasion and thermodenudation are active in the study area. During the summer, the thawing is continuous, and slumped materials accumulate on the beach. Figure:16 depicts the wave-cut niche at the base of the bluff at profile#11. The niche has not reached a critical length where the overhanging bluff is destabilised. The vertical position of the niche is higher than that at high tide. It was formed by the storm surge before the observation was made. Both thermoabrasion and thermodenudation are observed in the study area. No loose sediment was seen at the base or inside the niche opening during the observation period. The sediments must have been carried away by the return currents when the beach was flooded by the storm.

Figure 16: Status of Profile#11 during the 2015 measurement. The coastal profile is shown as a black line. A wave-cut niche is clearly visible at the base of the bluffs. Image source: SAMCoT Report, 2015.

The permafrost layer inside the bluffs during the summer is shown in Figure:17. The thawed layer above the permafrost is approximately 0.5 to 1 m at the bluff surface. It is clear from the figure that the thawed layer has a considerable thickness at the bluff slope. We can infer that the intensity of the slumping (mass flux) is the limiting process. All the thawed layers did not slump towards the base. In other words, the thawing rate (dx_t/dt) can be higher than the reduction rate of the thawed layer (dz/dt) due to slumping.

Figure 17: Permafrost inside the bluff excavated during the field investigation in 2018. Image source: Gorshkov, SAMCoT Report 2015

The following summarises the observations in general:

- Thermodenudation at the bluff face may be active, even when sea ice is present, and land-fast ice remains in the base of the bluffs. Unlike thermoabrasion, the open water season is thus not a prerequisite for thermodenudation.
- The thawed sediments from the bluffs fall on gravity and expose the permafrost underneath it. The slumped materials are loose and accumulate on the beach.
- Wave-cut niches are developed at the base of the bluffs, while the bluffs may still be stable. It may take several storms to elongate the niche depth to a critical depth. Unless the niche depth reaches the critical length, the bluff remains stable.
- The active organic layer under the vegetation shows greater resistance against erodibility.
- Thawed sediments accumulated at the base of the bluffs remain there until an extreme event creates a higher water level and return current.

4 Calibration of the Model

Some of the model input parameters, such as critical slope (m_{cr}), convective heat transfer coefficient (h_c), water level (wl), and tensile strength of permafrost (c), are usually site specific. We calibrate the model's input parameters using field measurements from zones S#1 and S#2 of the study area. We use the measurements from 2015 and 2016 to calibrate the model. One case from S#1 and S#2 is chosen. Both cases are separately calibrated since the profiles are considered mutually exclusive. The two zones are different in geometry (bluff height and bluff face slope) and geological settings, so we expect some input parameters to be different. However, the water level at the outer nearshore boundary BC2 is the same for both cases.

4.1 Domains of interest for calibration of the model

4.1.1 Time

We conducted one field investigation each year, so the numerical model could not be calibrated for less than one year (i.e., it is not possible to calibrate the model based on summer alone). The erosion estimated from the measurements is also a mix of thermodenudation and thermoabrasion; we cannot calibrate the two mechanisms of thermoabrasion and thermodenudation separately. We typically have measurements near the end of the summer (middle of September). The winter begins three to four weeks after the measurements are taken.

4.1.2 Space

The intent of the calibration process of the numerical model is to simulate the morphological changes at the bluffs and the beaches as close as possible to the measurements. The indicators of erosion measurements, such as (a) crest retreat, (b) erosion volume and (c) the slope of the bluff face, are the targets. The morphological changes in the coastal profile from the shoreline to the bluffs are considered for calibration. Out of the three erosion indicators, the primary target is to simulate erosion by volume, i.e., the volumetric changes between the two measurements of consecutive years. We measure erosion as volume changes from the shoreline until 15 metres from the cliff towards the land. The erosion measurement is the volume per metre along the shore parallel line ($m^3/m{-}width$). The following equation is used to determine the erosion:

$$E = \sum_{i=n}^{N} \frac{1}{2}\Delta x[(\alpha_i + \alpha_{i+1}) - (\beta_i + \beta_{i+1})] \tag{13}$$

where E is the erosion, n is the grid point at the shoreline, N is the grid point 15 metres from the cliff point, Δx is the horizontal distance between two grid points, α is the measurement of the previous year and β is the measurement of the current year. A positive value of E represents erosion, whereas negative values indicate accretion. We used 'net erosion' to describe the arithmetic sum of erosion and accretion.

4.2 The case studies for the calibration

We choose two cases as described in Table:2 for the calibration. The case studies are termed case#1 and case#2. Both cases are from the same period. The coastal profiles of the cases are shown in Figure:18 and 19.

Table 2: A summary of the two cases for the calibration.

cases	zone	profile	Time		Crest retreat	Erosion	Accretion	Net Erosion
			From	To	(m)			($m^3/m - width$)
case#1	S#1	P#1	15-09-2015	14-09-2016	4.1	10.31	3.28	7.04
case#2	S#2	P#8	15-09-2015	15-09-2016	2.9	0.00	12.51	12.51

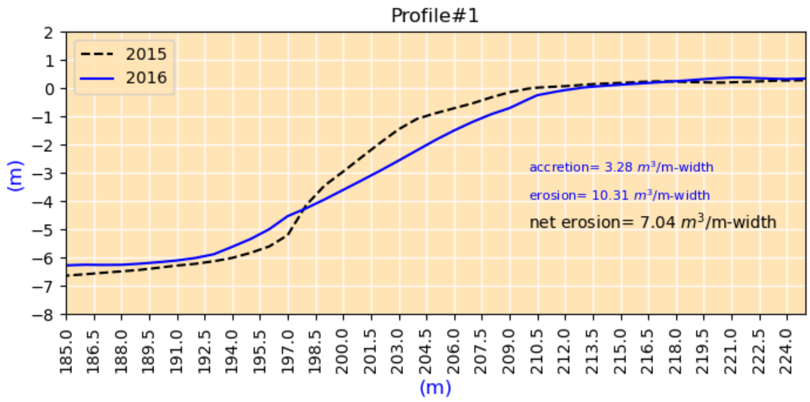

(a) case#1: the measurements of profile P#1, from 2015 to 2016.

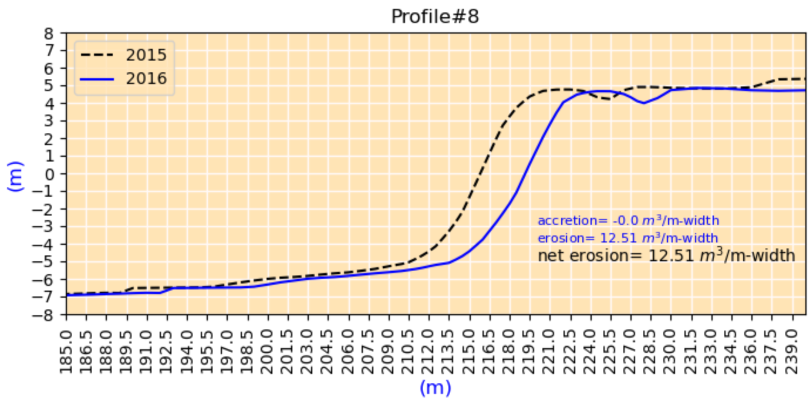

(b) case#2: the measurement of profile P#8, from 2015 to 2016.

Figure 18: The coastal profiles of cases #1 and #2 are shown.

The cases started in September 2015 and ended in September 2016. The summers of 2016 and 2017 are among the hottest summers in recent decades. We can make the following observations about the cases:

1. the bluff height for case#1 is 6 metres, and for case#2 is 13 metres. The bluff slope of case#1 is approximately 0.4, which is lower than the bluff slope of case#2 (0.9).
2. The cases demonstrate different erosion patterns. For case#1, we note that the profile has undergone both erosion and accretion; the value of erosion is almost three times the value of accretion (Figure:18a). The accretion value indicates that the sediments accumulated in the lower part of the bluffs. No accretion is measured for cases#2(Figure:18b). For case#2, all the sediment from the erosion must have been washed away offshore.
3. The crest retreat for case#1 is 4.1, which is larger than that of case#2, even though the erosion volume of case#1 is lower. Because of the higher bluff heights (13 m vs. 6 m) for a similar crest retreat, case#2 should have twice the erosion volume.

4. The changes in the bluff slope are negligible for case#2 but significant for case#1. For case#1, the bluff base did not retreat; instead, the crest retreated, and the bluff slope was lowered due to erosion.

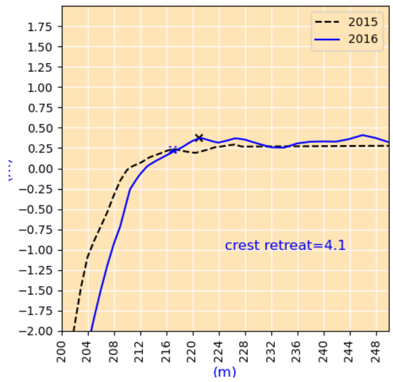

(a) case#1: crest retreat.

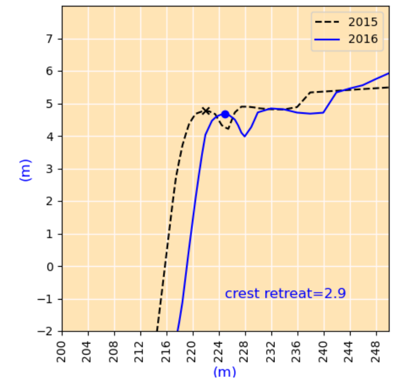

(b) case#2: crest retreat.

Figure 19: The crest retreat of case#1 and #2 are shown.

4.3 Environmental forcing

The wind speed, air temperature, and water temperature from September 2015 until September 2016 are shown in Figure:20. The air and the sea-surface temperature have almost no phase lag. The wind speeds are higher during the winter. The summer of 2016 was relatively calm, indicating that the thawing process (thermodenudation) dominated the erosion. The air temperature during the summer of 2016 reached 28 °C, which is a significant anomaly. The source of these input parameters is the NOAA reanalysis model (Saha et al., 2014).

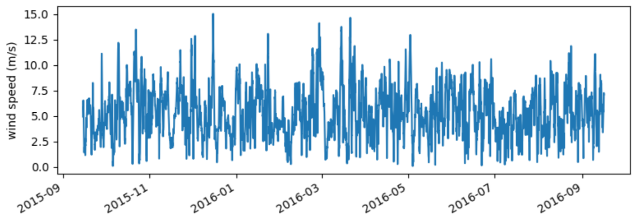

(a) Wind speed in the study area. The winter storms have higher magnitudes. Data source: NCEP, NOAA.

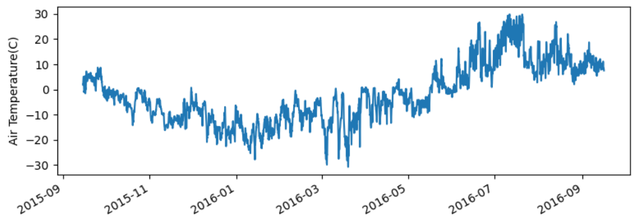

(b) The air temperature of the study area during the summer of 2016 reached 28°C. The year 2016 was the hottest year in recent decades. Data source: NCEP, NOAA.

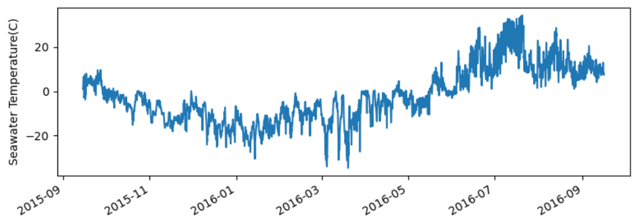

(c) Sea-surface temperature. Data source: NCEP, NOAA.

Figure 20: The environmental forcing during the calibration cases is shown.

4.4 Calibrated parameters

Both cases are from the same time period, so the input parameters, such as wind speed, air temperature, and water temperature, are the same for both cases. The physical distances between the profiles are approximately two kilometres, so we assumed no phase lag in water levels. The water level is also constant during the calibration for the cases. A brief description of the calibrations of the parameters is given below. A summary of the calibrated values of the parameters is shown in Table:3.

Table 3: Summary of the calibrated parameters.

parameter	zone	symbol	calibrated value	unit	remarks
convective heat transfer coefficient (air)	S#1 & S#2	$h_{c;surface}$	90	W/m^2-k	for bluff surface
	S#1 & S#2	$h_{c;face}$	98	W/m^2-k	for bluff slope
	S#1 & S#2	$h_{c;beach}$	120	W/m^2-k	for beach
convective heat transfer coefficient (water)	S#1 & S#2	$h_{c,w}$	700	W/m^2-k	for seabed
Tensile strength of ice	S#1 & S#2	c_{ice}	1×10^4	N/m	
Tensile strength of permafrost	S#1 & S#2	c_p	1.2×10^5	N/m	
critical slope (dry)	S#1	$m_{cr;a}$	0.35	-	
	S#2	$m_{cr;a}$	0.5	-	
critical slope (wet)	S#1 & S#2	$m_{cr;w}$	0.2	-	
mean water level	S#1 & S#2	h_m	-7.7	m	Ref:GSK-2011[2]

4.4.1 Calibration of the water level

The water level (wl) at boundary BC2 (see Figure:3) is updated at every timestep. We estimate wl at the BC2 boundary by superimposing water level changes due to tide and storm surge on the mean water level (h_m). At the BC2 boundary, the water level (wl) is treated as the boundary condition for the nearshore module, expressed by the following equation:

$$wl(t) = h_m + h_t(t) + \eta(t) \tag{14}$$

where h_m is the mean sea level, which is constant during the simulation (not a function of time), h_t is the water level changes due to tide at three-hour intervals (interpolated from the measurement), and η is the storm surge level estimated at three-hour intervals by the storm surge submodule. For calibration, we use the field measurements of water level using the Russian State Geodetic Coordinate System (GSK-2011), which is also used as a datum for the numerical model. The values of h_t and η are not subject to calibration. However, the final value of h_m for the model is obtained by iterations. We use the initial iteration value for h_m from the field measurements during the calm summer days. The iteration values of h_m are chosen within the range. The upper and lower limits are the constraints imposed from field observations: (1) the water level does not touch the base of the bluffs during high tide on a calm day (upper limit of h_m), and (2) the length of the beach from the base of bluffs to the swash zone varies from 40 to 70 metres (lower limit of h_m). After several iterations, we calibrate the value of h_m at -7.7 metres for both cases.

4.4.2 Calibration of the convective heat transfer coefficient

The convective heat transfer coefficient is different for the four sections (see Figure 4). As a starting point for the h_c values for water, we follow the model of Kobayashi et al. (1999) as follows:

$$h_c = \frac{a f_w C_w U_w}{1 + F\sqrt{0.5 f_w}} \tag{15}$$

where a is the empirical parameter equal to 0.5, f_w is the wave friction factor, C_w is the volumetric heat capacity of seawater, U_w is the fluid velocity and F is the parameter depending on the turbulence and Prandtl number. Kobayashi et al. (1999) estimated the value of h_c within the range of 500 to 800 $W/m^2{-}k$. After several iterations, we reach $h_{c,w} = 700W/m^2 - k$ for our cases.

For the h_c of air, the initial value of iteration is determined by using the equation for the forced convection of a turbulent flow over a flat plate:

$$N_u = \frac{h_c \cdot L}{k_f} = 0.037Re^{0.8}Pr^{1/3} \tag{16}$$

where N_u is the Nusselt number, k_f is the thermal conductivity of the fluid, L is the characteristic length, Re is the Reynolds number, and Pr is the Prandtl number. Using Pr=0.71 for air, we estimate the initial value of h_c to be approximately 25 $W/m^2{-}k$. However, this value of h_c for air limits the thawing depth and does not agree with our field measurements. The calibrated values of h_c of air for the three sections are chosen between 90 and 120 (Table:3).

4.4.3 Calibration of the critical slope

The slumping process inside the numerical model is controlled and triggered using one single parameter, the critical slope, as mentioned in Eq. 8. The equation is valid for the dry and wet parts of the profile. The field measurements show that the slope of the profiles at the end of the summer varies from 0.1 to 1.1 (Figure:21). A distinct difference is visible between the bluff slopes of zones S#1 and S#2. The values of m_{cr} are determined by iteration for the two sites. The coastal profiles are measured at the end of the summer. When the thermodenudation for the summer is almost complete, we can infer that the slopes of the bluff faces are stable slopes, and thus, the critical slope should be more than these measured slopes. We also note that the profiles at S#2 have a greater bluff height and steeper slope. After the calibration, we find that the $m_{cr,a} = 0.34$ for S#1 and $m_{cr,a} = 0.52$ for S#2 for the dry part of the coastal profiles are the most suitable values. However, we derived these values by iterations, not from field measurements. For the submerged portion of the coastal profiles, we used $m_{cr,w} = 0.2$.

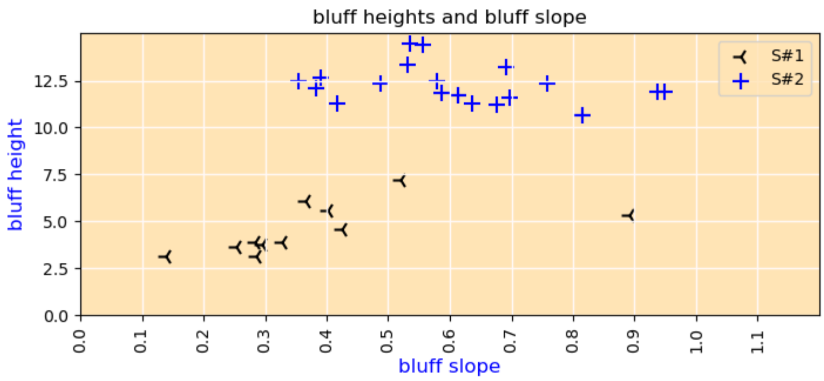

Figure 21: The relation of the bluff height and bluff slope in the study area.

4.5 Result of calibration

Using the above mentioned calibrated input parameters and forcing the model with the environmental data shown in Figure:20, the results are in good agreement with the measured erosion volume, as shown in Figure:22 and 23. A summary of the results of the calibration is shown in Table:4. The numerical model overestimates the erosion for both cases. For crest retreat, the model underestimates for case#1 and overestimates for case#2.

Table 4: Summary of the calibration cases.

case	criteria	measured	simulation	error (%)
case#1	erosion volume ($m^3/m - width$)	7.04	8.3	17.9%
	crest retreat (m)	4.1	2.9	29.3%
case#2	erosion volume ($m^3/m - width$)	12.51	14.8	18.3%
	crest retreat (m)	2.9	4	37.9%

4.5.1 Prediction of erosion

For case#1, the simulated erosion volume and crest retreat differ from the measurements by 17.9% and 29.3% respectively. The simulation results of the cumulative erosion are shown in Figure:22b. The results show that the erosion for case#1 is mostly thermoabrasion. The collapse occurred three times, and all the collapses are shear failures (expressed by Eq. 10). The model requires thawing depth as an initial condition. We calibrate the model with 0.35 metres of initial thawing depth. The thawing depth at the bluff surface by the simulation is shown in Figure:22a. Thawing depth had a small initial increase followed by a sharp decrease due to winter. The numerical model estimates no thawing depth from January until almost the end of May. No erosion is recorded for this period. The inundation depth, h_{id} is shown in Figure:22c. Our numerical model requires at least 10 cm of water sustained for at least three hours to trigger the niche submodule. We notice many instances of positive h_{id}, especially during the early part of summer (from May to September). The largest storm surge occurred during May, which did not result in any collapse. The thermal driving force of niche growth: the temperature of the water was not warm enough to rapidly grow the niche. The h_{id} values are spiked and not continuous, which is in line with our assumption that only during storm surges can water reach the base of the bluffs. The sudden jumps in the cumulative erosion values indicate a bluff collapse by thermoabrasion. We deduce from the pattern of the cumulative erosion that the erosion at this profile is dominated by thermoabrasion.

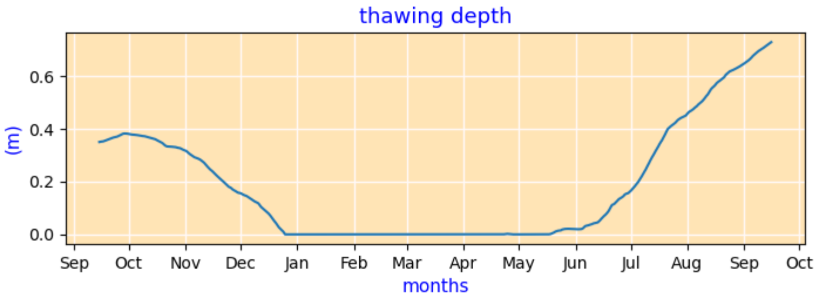

(a) The thawing depth at the bluff for Case#1.

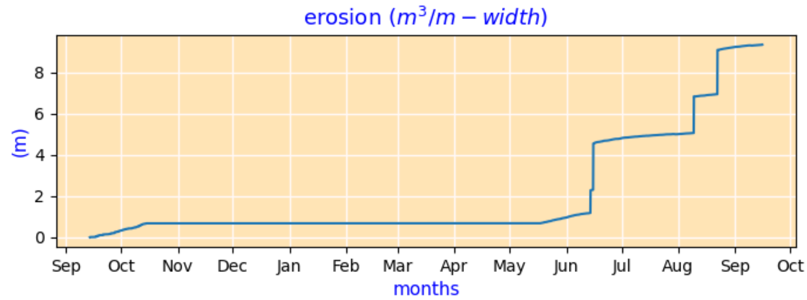

(b) The cumulative erosion on profile#1 for case#1.

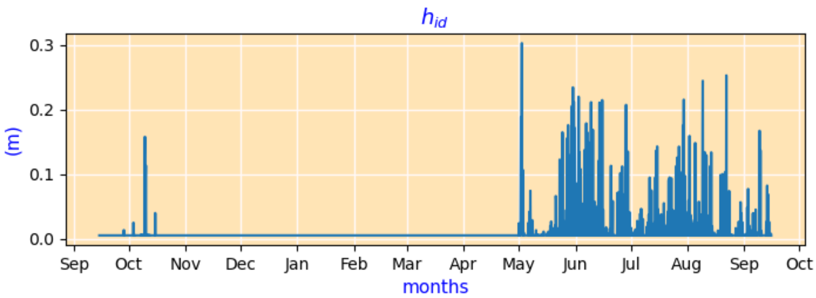

(c) Water depth at the base of the bluff, h_{id}

Figure 22: Results of the calibrated model of Case#1. The erosion volume from the measurement was $24m^3/m - width$.

For case#2, the simulated erosion volume and crest retreat differ from the measurements by 18.3% and 37.9%, respectively. A similar thawing depth pattern is estimated for case#2 since the environmental forcings are precisely the same (Figure:23a). The h_{id} values are lower for case#2, as the beaches of S#2 are slightly higher (approximately 20 cm). The cumulative erosion for case#2 is also different; the erosion is not dominated by thermoabrasion, as seen for case#1. The simulation records two collapses. The thermodenudation is stronger for case#2. The bluff collapses between the two cases do not occur during the same storms. The model behaved this way, as the h_{id} values are estimated to be small for case#2, resulting in very slow niche growth. On the other hand, the bluff face has a steeper slope, and the model estimates more slumping for case#2.

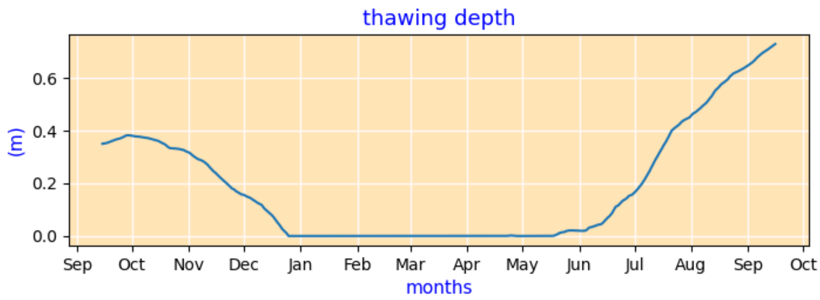

(a) The thawing depth at the bluff for Case#2.

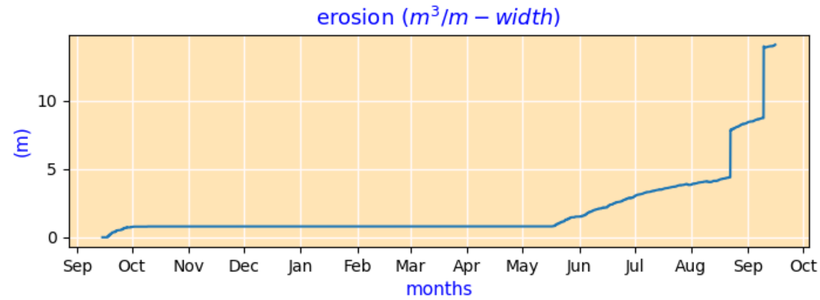

(b) The cumulative erosion on profile#8 for case#2.

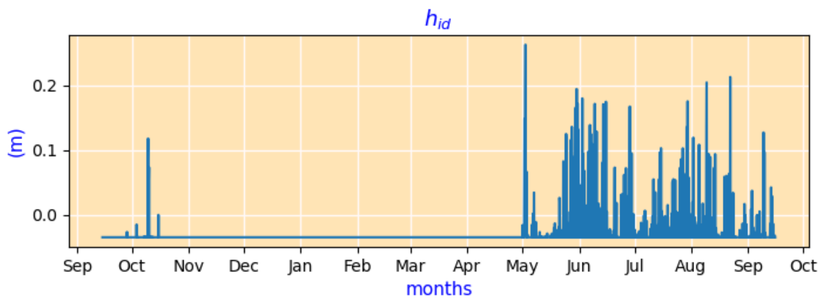

(c) Water depth at the base of the bluff, h_{id}

Figure 23: Results of the calibrated model of Case#2. The erosion volume from the measurement was $15m^3/m - width$.

4.5.2 Prediction of crest retreat

The secondary aim of the simulation is to predict the crest retreat of the bluffs. The crest retreat of the Arctic coast is retrogressive, i.e., always retreating as there is no restoration mechanism like the dune systems of the sandy beaches of warmer climates. The crest of the bluff is always moving towards the land. The annual crest retreat rate is of particular interest for the prediction of vulnerability and associated risks. For cases #1 and #2, the crest retreat rates were 4.1 and 2.9 metres, respectively. The model predicts crest retreats of 2.9 and 4 metres for the cases. The model both underestimates and overestimates the crest retreats.

4.5.3 Prediction of the shape of coastal profile

Another secondary aim of the calibration is to forecast the shape of the profile at the bluff face and the elevation of the beach. The elevation of the beach is important since it affects the inundation depth (h_{id}), which in turn controls the thermoabrasion. The performances of the model for case#1 and case#2 are shown in Figure:24 and 25. We used the root mean square error (RMSE) to indicate deviation from the measurements. Before estimating the RMSE value, we 'normalise' the profile around the middle of the bluff slope. Hence, the RMSE values are only related to the shape of the profile, not associated with the position of the bluff. The equation to calculate the RMSE values is as follows:

$$\mathrm{RMSE} = \sqrt{\frac{\sum_{i=1}^{N} \left(o_i - \hat{s}_i\right)^2}{N}} \tag{17}$$

where RMSE is the root mean squared error, i is the variable, N is the number of grid points, o is the measured value at the grid point and s is the simulated value at the grid point.

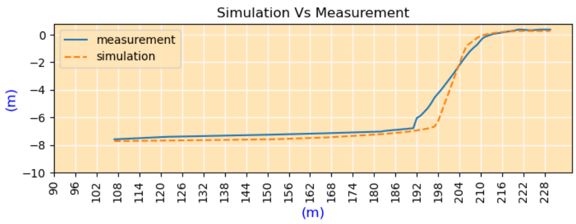

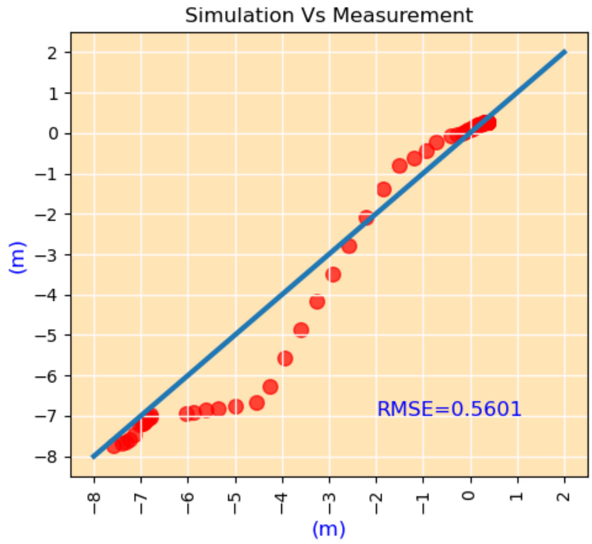

Figure 24: case#1: prediction of the shape of the coastal profile after normalising the simulation around the middle of the bluff slope. The RMSE of the prediction is 0.56 m.

For case#1, we observe that the simulation predicted a slope slightly steeper than the measurement. The simulation predicted that the elevation of the beach was close to the measurements, albeit it overestimated the erosion by sediment transportation. The deviation is highest near the base of the bluff; errors near the beach are negligible. However, the model overestimates the erosion at the base of the bluffs.

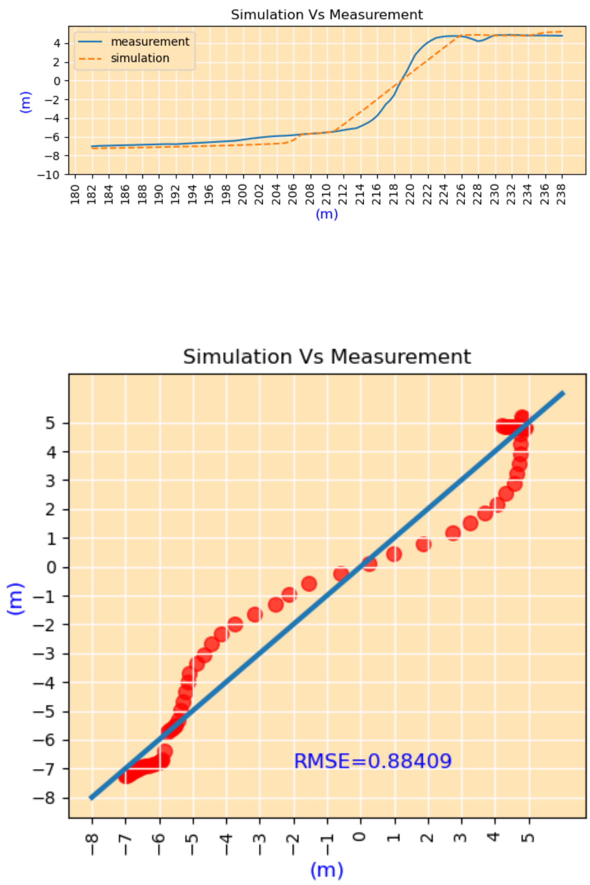

Figure 25: case#2: prediction of the shape of the coastal profile after normalising around the middle of the bluff slope. The RMSE of the prediction is 0.88 m.

For case#2, the model simulates the slope as much as the prediction. The simulated values deviated near the cliff points and the bluff base. The prediction at the beach was close. The RMSE values are higher for case#2.

5 Validation

After calibrating the numerical model, we apply the calibrated model to another three sets of measurements to validate the model. The new cases are summarised in Table:5. Case#3 and case#4 are from profiles#1 and #8 for 2016-2017. Case#5 is from the two measurements of 2012 and 2017 on profile#1. Case#5 is selected to examine the performance of the numerical model for simulating long-term erosion. The measured erosion volume and crest retreats of all the cases are shown in Figure:26. A summary of the erosion and crest retreat is provided in Table:5.

Table 5: A summary of the three cases for the validation.

cases	zone	profile	Time		Crest retreat	Erosion	Accretion	Net Erosion
			From	To	(m)			$(m^3/m - width)$
case#3	S#1	P#1	15-09-2016	14-09-2017	3.2	28.73	0.00	28.73
case#4	S#2	P#8	15-09-2016	15-09-2017	3.9	11.81	0.00	11.81
case#5	S#1	P#1	13-06-2012	15-09-2017	16	71.05	0.00	71.05

Even though Case#1, #3 and #5 are on the same profile#1, the erosion pattern is different for each case. In two consecutive years, the erosion pattern drastically changed between cases #1 and #3 (Figure:26a). The bluff slope of case#3 morphed into an uneven bluff slope. The bluff slope became steeper at the lower part near the bluff base, indicating that during the summer of 2017, the hydrodynamic forcing removed a large volume of sediments from the bluff base. Case#4 on profile#8 is relatively stable, but we note the lowering of the elevation of the beach (Figure:26b). Lowering beach elevation indicates that the beach was inundated frequently during the summer of 2017, a similar conclusion we made for case#3. Case#5 is a representation of long-term erosion (Figure:26c). The erosion of the beach was significant in this case; the profile is lowered by approximately 1.5 metres around the 180-metre mark. However, the base of the bluffs remains almost at the same level. No positive accretion value was recorded for any of the three cases, which suggests that the accumulated sediments must have been washed away by hydrodynamic forcing.

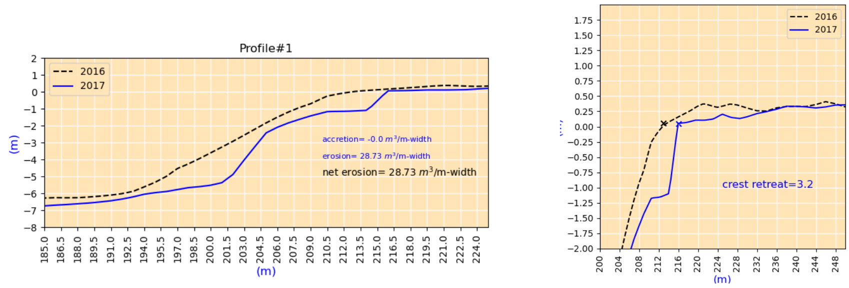

(a) case#3: the measurements are of profile P#1, from 2016 to 2017.

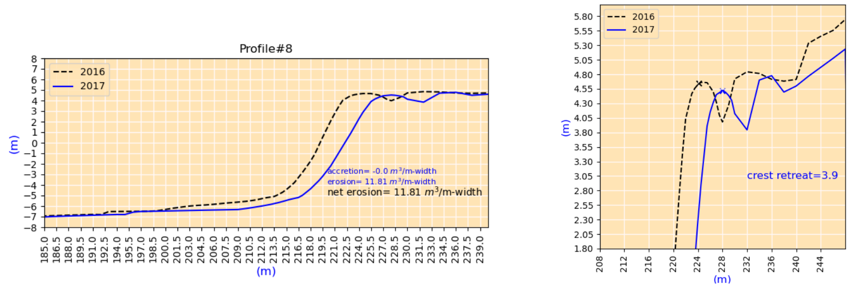

(b) case#4: the measurement of profile P#8, from 2016 to 2017.

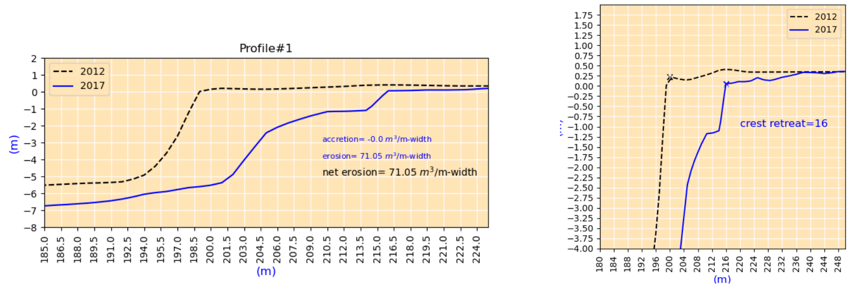

(c) case#5: the measurement of profile P#1, from 2012 to 2017.

Figure 26: The coastal profiles of case#3, #4 and #5 are shown.

5.1 Methodology of the validation

The parameters that were calibrated in Table:3 are used without any changes. The time series of the input parameters air and water temperature, wind speed and tides are updated. The initial thawing depths for case#3 and case#4 are used from the previous simulations (the thawing depth of the last timestep for case#1 and case#2). For case#5, the initial thawing depth was taken as zero because the case starts in June, not in September. From the thawing depth patterns of cases #1 and #2, we estimate that the thawing depth in June is zero.

5.2 Results of validation

A summary of the results of the simulation is shown in Table:6. The results show a good agreement with the measurements.

Table 6: Summary of the validation cases.

case	criteria	measured	simulation	error (%)
case#3	erosion volume ($m^3/m - width$)	28.73	25.8	10.2%
	crest retreat (m)	4.1	3.9	4.8%
case#4	erosion volume ($m^3/m - width$)	11.81	15.1	27.8%
	crest retreat (m)	3.9	4.8	23.1%
case#5	erosion volume ($m^3/m - width$)	71.05	80.5	13.3%
	crest retreat (m)	16	4 14.8	7.5%

5.2.1 Thawing depths

The thawing depths for case#3 and #4 are identical (shown in Figure:27a). An initial small increase in the thawing depth means that the measurements were not taken at the end of summer. The end of summer coincides with the highest thawing depth. The thawing depth pattern for case#5 is shown in Figure:27b. The maximum thawing depth varies each year; the pattern indicates that the summer of 2017 was the warmest. The thawing depth varies from 0.4 to 0.8 metres, which agrees with the field observations.

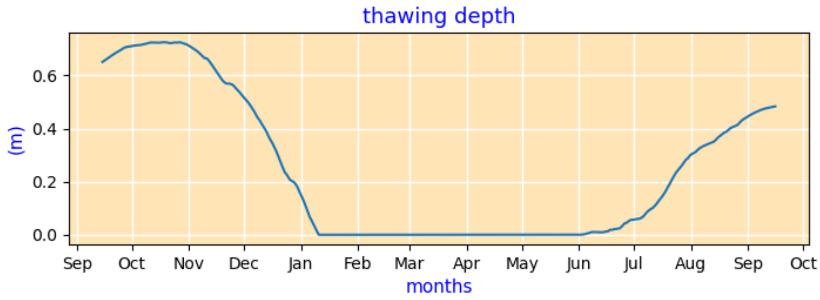

(a) The thawing depth of case#3 and #4.

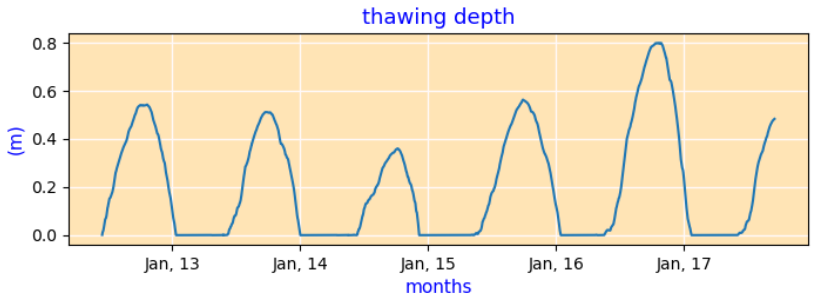

(b) The thawing depth of case#5

Figure 27: The coastal profiles of case#3, #4 and #5 are shown.

5.2.2 Validation of case#3

A summary of the validation results is shown in Figure:28. The cumulative erosion of the profile reaches 25.8 $m^3/m{-}width$, which is slightly underestimated by the simulation (Figure:28a). The erosion is dominated by thermoabrasion, but the contribution from thermodenudation increased significantly from the previous year (case#1). The rate of thermodenudation was strong during the summer of 2017. However, the prediction of the beach elevation deviated from the measurements (Figure:28b). The shape of the bluff face was irregular, which the model failed to capture. Similar to the other cases, the deviation is higher near the base.

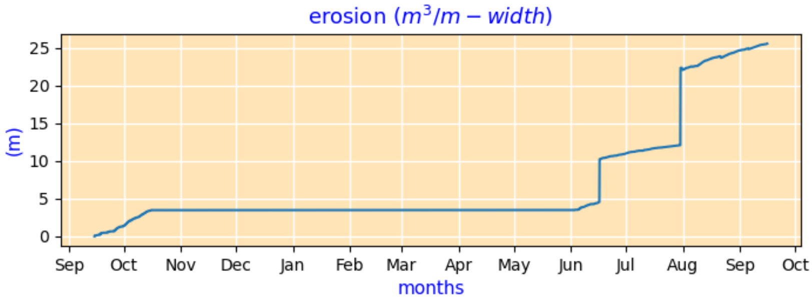

(a) case#3: cumulative erosion.

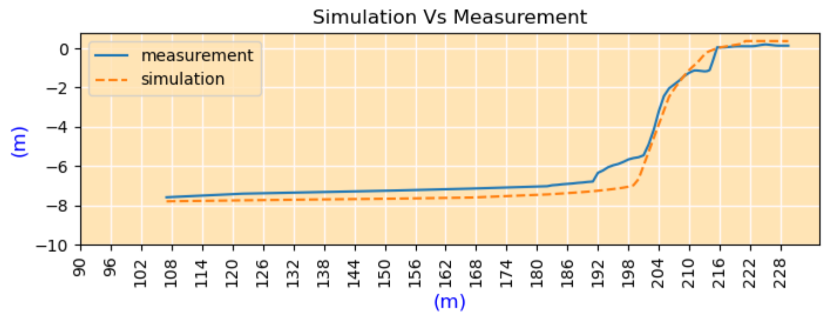

(b) case#3: the simulated profile after normalising.

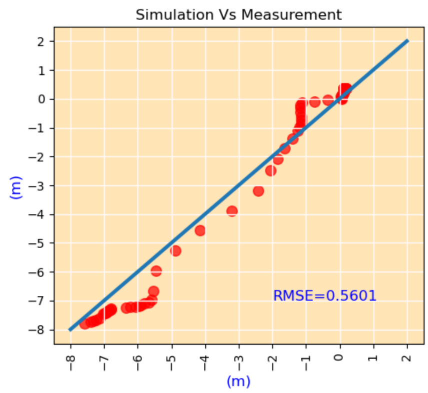

(c) case#3 The deviation of the simulation from the measurements, the RMSE value is 0.561

Figure 28: Validation results for case#3.

5.2.3 *Validation of case#4*

The cumulative erosion volume simulated by the model for case#4 is shown in Figure:29a; the erosion is dominated by thermoabrasion. The model estimated an erosion volume of 15.1 $m^3/m{-}width$, which is overestimated from the measurement of 11.81 $m^3/m{-}width$. The simulated shape of the profile and the measurement are shown in Figure:29b, and the RMSE value was found to be 0.9409.

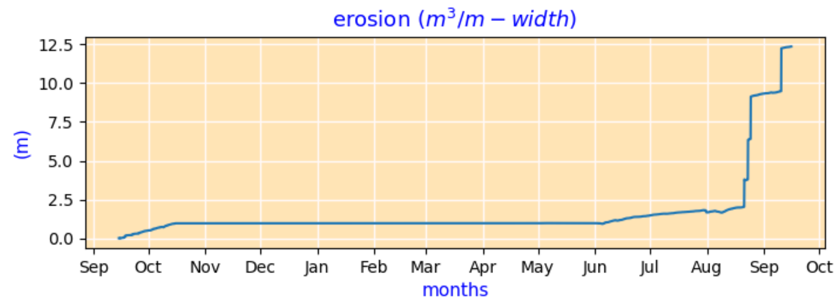

(a) case#4 validation

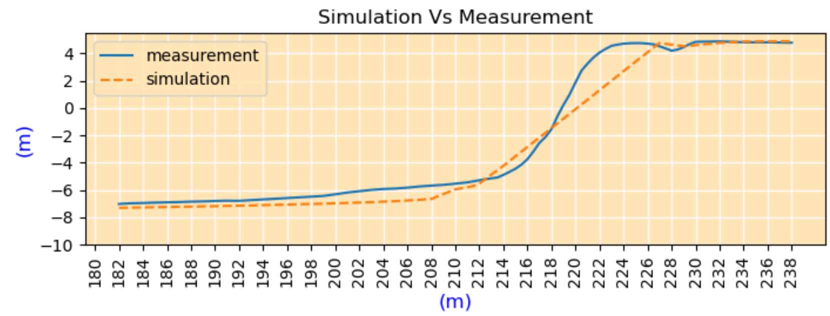

(b) case#4: the simulated profile after normalising.

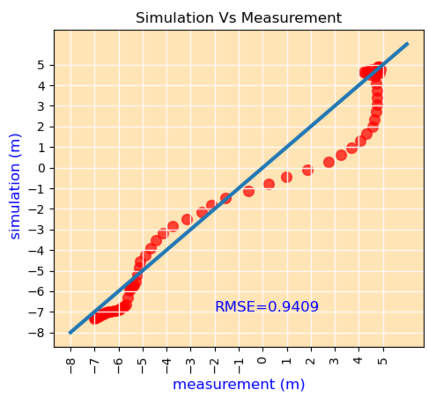

(c) case#4 The deviation of the simulation from the measurements, the RMSE value is 0.9409

Figure 29: Validation results for case#4.

5.2.4 Case#5: Simulation of long-term erosion

The application of the model for the long-term erosion simulation is demonstrated by case#5. The simulation duration of the case is five years and four months. The results of the simulation are shown in Figure:30.

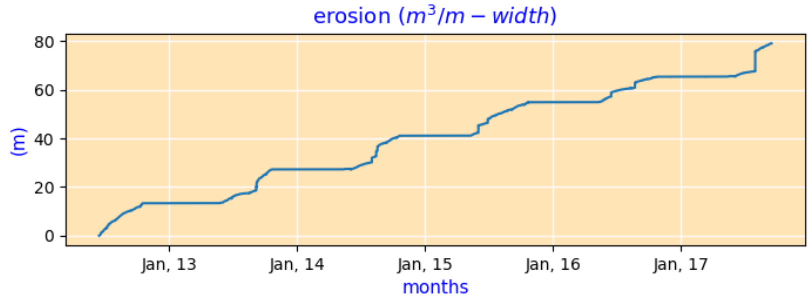

(a) Cumulative erosion for case#5.

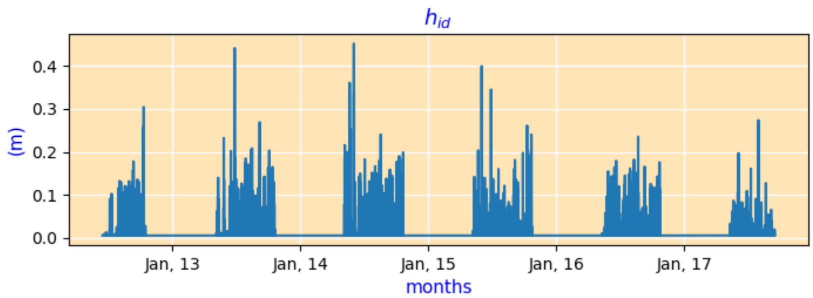

(b) The h_{id} values over the simulation time.

Figure 30: Validation results for case#5.

The erosion pattern of case#5 is similar to the other cases. The erosion is dominated by thermoabrasion. The thermodenudation rate is different each year. The h_{id} values during the simulation are shown in Figure:30b. We observe higher h_{id} values for the earlier years; the highest h_{id} is observed during the summer of 2014. The effect of the h_{id} did not translate to bluff collapse. The bluff collapse by niche growth requires a positive h_{id} value, but the intensity of the erosion does not depend on the frequency and magnitude of the h_{id} values.

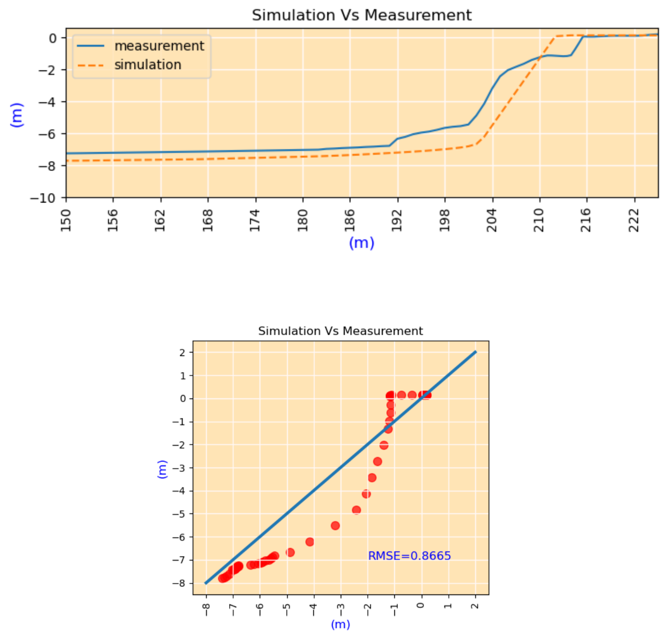

Figure 31: The shape of the profile after normalising. The RMSE value was estimated to be 0.86.

The deviation of the profile shape is shown in Figure:31. The deviation is higher at cliff points and bluff bases. During the five-year simulation, the beach elevation was simulated to be lower than the measurements; the deviation was nearly 0.3 metres, whereas the average deviation at the grid points was 0.86 metres (RMSE).

In Figure:32, the air temperate and simulated cumulative erosion are drawn. The upwards zero crossing of the air temperature and the inception of the erosion in the summer have a small phase lag. The erosion rate correlates with air temperature; higher air temperature leads to increased erosion. At the end of the summer, the erosion stops as soon as the air temperature has the downwards zero crossing.

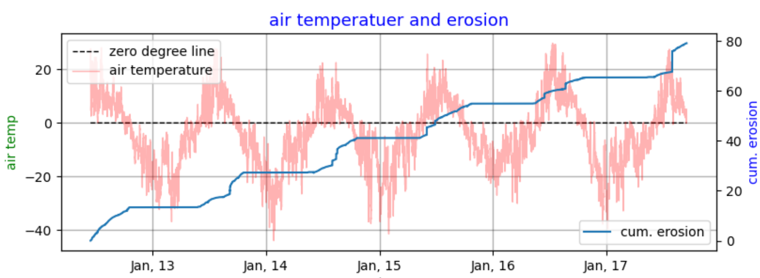

Figure 32: Air temperature and cumulative erosion(simulation).

The thawing index of air is used in many empirical equations concerning the thawing of permafrost and erosion. Figure:33 draws the measured cumulative thawing index of case#5 juxtaposed with the simulated cumulative erosion. The correlation between the two parameters is very strong even though the thawing index is only one of the environmental forcing parameters of erosion. The cause of the erosion can be partly attributed to the thawing index. We cannot establish a direct causation-relation of the thawing index of air with thermoabrasion; warm air has almost no immediate effect on erosion by thermoabrasion. From the simulation result, we notice that even though the erosion is dominated by thermoabrasion, a strong correlation exists between the cumulative thawing index and cumulative erosion.

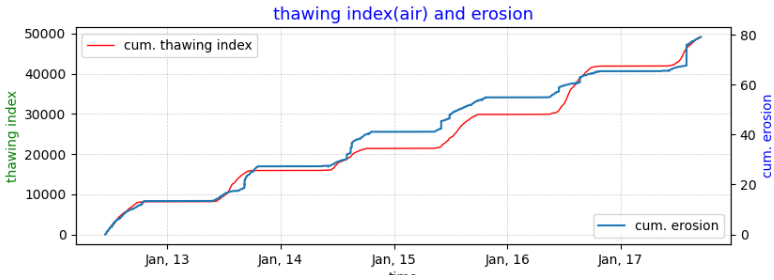

Figure 33: Cumulative thawing index and erosion(simulation).

However, the wind speed and the simulated cumulative erosion of case#5 are not correlated. The wind speeds are higher during the winter when there is no erosion. The bluff collapses (creating a jump on the cumulative erosion) rarely coincide with the storms of the summer. We can infer that the bluff collapse by thermoabrasion is not dominated by storms in the summer; instead, a combination of various environmental forcings results in bluff failure, justifying the inclusion of hydrodynamic and morphological submodules into the numerical model of Arctic coastal erosion.

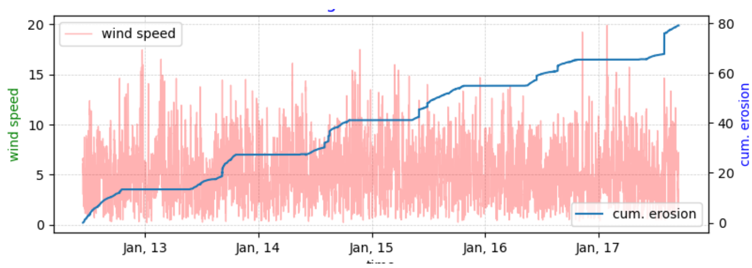

Figure 34: Wind speed and cumulative erosion (simulation).

6 Conclusion

In this paper, we describe a comprehensive process-based model that simulates Arctic coastal erosion, which includes hydrodynamic forcing from the sea. The model is divided into three modules: offshore, nearshore and bluffs. The physical processes are included in the model as submodules under the three modules. A feedback mechanism is established between the submodules. The hydrodynamic forcing and related morphological changes are simulated by XBeach. The model can simulate thermodenudation and thermoabrasion simultaneously.

The numerical implementation of the model is described briefly, and the workflow is explained. We calibrate the model using field measurements from Baydaratskya Bay in the Kara Sea, Russia. The study area was surveyed every year starting from 2012. The following conclusions can be made from the calibration process of the numerical model:

1. The erosion during the winter is negligible to none.
2. There is a slight phase lag between the commencement of summer (measured by air temperature) and the beginning of slumping. The air temperature had an upwards zero crossing at the end of May, but thawing began after June for both cases #1 and #2.
3. Smaller sudden spikes in air and water temperatures at the beginning of the summer do not contribute to thermodenudation. The model also does not show any immediate response to the spikes of temperature anomalies. This behaviour indicates that the limiting factor for thermal energy transfer and thawing of permafrost is the energy requirement for the latent heat of transformation of ice to water.
4. thermodenudation is continuous and of lower intensity, whereas thermoabrasion causes spikes in the erosion volume.

The model is validated by another three sets of observations, two short term (one year) and one long term (five year). We demonstrate that the model can simulate long-term erosion with the same level of fidelity. We infer the following concluding remarks from the results of simulations:

1. The results of the numerical model suggest that thermoabrasion is a complex process and does not demonstrate a linear relation with the intensity of storms. In other words, the largest storm does not necessarily lead to a collapse. A bluff collapse by a wave-cut niche is a combination of the nearshore beach profile, storm surge duration, temperature of the water and geometry of the bluff.
2. The two consecutive bluff collapses routinely have an interval between them, and the time lapse between the two collapses is four to six weeks. The sediments released from the collapsed bluff change the elevation near the swash zones, which reduces the probability of inundation of the beach by warm water, resulting in slow niche growth.
3. The parameter inundation depth, h_{id}, acts as an on-off switch for thermoabrasion; however, the numerical model does not show a relation between the magnitude of h_{id} and erosion.
4. The erosion rate of thermodenudation was found to be approximately 0.4 $m^3/month$ for low bluff height profiles in zone S#1. The erosion rate by thermodenudation for the zones with high bluff was estimated to be close to 1 $m^3/month$. The erosion rate of thermodenudation does not show a strong relation with the thawing depth (x_t).

We demonstrate that coupling the physical processes as submodules to simulate erosion of the Arctic coastal erosion model can produce realistic coastline erosion rates. It is possible to couple the model with globally available climate reanalysis data. The simulation results are within the same order of magnitude as the field measurements. The model can be further improved by considering the following:

6.1 Future development

1. The accumulation and melting of snow and related water flow are not exclusively modelled. Since there is no open water during the winter and the erosion of the coast is negligible, we did not model the effect of the snow. A snow module will improve the accuracy of the model.
2. The presence of sea ice was considered in a binary mode, where we ignored sea ice when the ice concentration was less than 20%, and it was assumed to have no effect on the waves. The damping effect of the floating ice on the waves may also improve the model's fidelity.
3. The critical slope (m_{cr}) is taken as depth-averaged for the profiles. One depth-averaged value is estimated for each zone in the study area. A matrix of m_{cr} values at different depths and different geometries will increase the accuracy of the model.
4. The collapse of the bluff is predetermined. A finite element model at the bluff face may better predict the irregular bluff slope.

Acknowledgments

The toolbox developed by the OpenEarth community (https://openearth.community/about-oec) helped us a lot and allowed better control over XBeach. The team under the leadership of Dr. Vladislav Isaev of the Department of Geocryology, Lomonosov Moscow State University (MSU), Russia supported the work and obtained the field observations with supports from the project Sustainable Arctic Marine and Coastal Technology (SAMCoT), Norway and Norwegian University of Science and Technology (NTNU). The report is written as part of the EU H2020-funded Nunataryuk project (Grant: 773421), where it is filed as part of deliverable 6.4.

References

Amante, C., & Eakins, B. (2009). Etopo1 1 arc-minute global relief model: Procedures, data sources and analysis. *NOAA Technical Memorandum NESDIS NGDC*.

Are, F., & Reimnitz, E. (2008). The a and m coefficients in the bruun/dean equilibrium profile equation seen from the arctic. *Journal of Coastal Research*(24 (10024)), 243–249.

Are F, E. (1988). Thermal abrasion of sea coast. *Polar Geogr. and Geol*, *12*, 1–157.

Atkinson, D. E. (2005). Observed storminess patterns and trends in the circum-arctic coastal regime. *Geo-Marine Letters*, *25*(2), 98–109.

Barnhart, K., Anderson, R., Overeem, I., Wobus, C., Clow, G. D., & Urban, F. E. (2014). Modeling erosion of ice-rich permafrost bluffs along the alaskan beaufort sea coast. *Journal of Geophysical Research: Earth Surface*, *119*(5), 1155–1179.

Barnhart, K., Overeem, I., & Anderson, R. S. (2014). The effect of changing sea ice on the physical vulnerability of arctic coasts. *The Cryosphere*, *8*(5), 1777–1799.

Barnhart, K. R., Anderson, R. S., Overeem, I., Wobus, C., Clow, G. D., & Urban, F. E. (2014). Modeling erosion of ice-rich permafrost bluffs along the alaskan beaufort sea coast. *Journal of Geophysical Research: Earth Surface*, *119*(5), 1155–1179.

Bogorodskii, P., Marchenko, A., Pnyushkov, A., & Ogorodov, S. (2010). Formation of fast ice and its influence on the coastal zone of the arctic seas. *Oceanology*, *50*(3), 317–326.

Booij, N., Haagsma, I., Kieftenburg, A., & Holthijsen, L. (2000). Swan implementation manual. *Delft University ofTechnology*.

Bull, D. L., Bristol, E. M., Brown, E., Choens, R. C., Connolly, C. T., Flanary, C., ... others (2020). *Arctic coastal erosion: Modeling and experimentation.* (Tech. Rep.). Albuquerque, NM (United States): Sandia National Lab.(SNL-NM).

Cohen, J., Screen, J. A., Furtado, J. C., Barlow, M., Whittleston, D., Coumou, D., ... others (2014). Recent arctic amplification and extreme mid-latitude weather. *Nature geoscience*, *7*(9), 627–637.

Dean, R. G., & Dalrymple, R. A. (1991). *Water wave mechanics for engineers and scientists* (Vol. 2). world scientific publishing company.

Deltares. (2022). *Xbeach.* Retrieved from `https://oss.deltares.nl/web/xbeach/about`

Frederick, J., Mota, A., Tezaur, I., & Bull, D. (2021). A thermo-mechanical terrestrial model of arctic coastal erosion. *Journal of Computational and Applied Mathematics*, *397*, 113533.

Galappatti, R. (1983). A depth integrated model for suspended transport. *Communications on hydraulics, 1983-07*.

Gibbs, A., Richmond, B., Erikson, L., & Jones, B. (2018). Long-term retreat of coastal permafrost bluffs, barter island, alaska. In *5th european conference on permafrost; eucop5: Chamonix, france* (Vol. 1, pp. 1–2).

Gibbs, A. E., & Richmond, B. M. (2015). *National assessment of shoreline change: Historical shoreline change along the north coast of alaska, us-canadian border to icy cape.* US Department of the Interior, US Geological Survey.

Guégan, E. (2015). *Erosion of permafrost affected coasts: rates, mechanisms and modelling* (Unpublished doctoral dissertation). Norwegian University of Science and Technology.

Günther, F., Overduin, P. P., Yakshina, I. A., Opel, T., Baranskaya, A. V., & Grigoriev, M. N. (2015). Observing muostakh disappear: permafrost thaw subsidence and erosion of a ground-ice-rich island in response to arctic summer warming and sea ice reduction. *The Cryosphere*, *9*(1), 151–178.

Harms, I., & Karcher, M. (1999). Modeling the seasonal variability of hydrography and circulation in the kara sea. *Journal of Geophysical Research: Oceans*, *104*(C6), 13431–13448.

Holland-Bartels, L., & Pierce, B. (2011). *An evaluation of the science needs to inform decisions on outer continental shelf energy development in the chukchi and beaufort seas, alaska* (Tech. Rep.). USA: US Geological Survey.

Hoque, M. A., Perrie, W., & Solomon, S. M. (2020). Application of swan model for storm generated wave simulation in the canadian beaufort sea. *Journal of Ocean Engineering and Science*, *5*(1), 19–34.

Hoque, M. A., & Pollard, W. (2008). Thermal and mechanical erosion along ice-rich arctic coasts. In *Proc., 9th intl. conf. on permafrost,(1)* (pp. 741–746).

Hoque, M. A., & Pollard, W. H. (2009). Arctic coastal retreat through block failure. *Canadian Geotechnical Journal*, *46*(10), 1103–1115.

Irrgang, A. M., Bendixen, M., Farquharson, L. M., Baranskaya, A. V., Erikson, L. H., Gibbs, A. E., ... others (2022). Drivers, dynamics and impacts of changing arctic coasts. *Nature Reviews Earth & Environment*, *3*(1), 39–54.

Irrgang, A. M., Lantuit, H., Manson, G. K., Günther, F., Grosse, G., & Overduin, P. P. (2018). Variability in rates of coastal change along the yukon coast, 1951 to 2015. *Journal of Geophysical Research: Earth Surface*, *123*(4), 779–800.

Isaev, V., Koshurnikov, A., Pogorelov, A., Amangurov, R., Podchasov, O., Sergeev, D., ... Kioka, A. (2019). Cliff retreat of permafrost coast in south-west baydaratskaya bay, kara sea, during 2005–2016. *Permafrost and Periglacial Processes*, *30*(1), 35–47.

Jones, B., Bull, D., Farquharson, L., Buzard, R., Arp, C., Grosse, G., & Romanovsky, V. (2018a). A decade of annual permafrost coastal observations indicate changes in the arctic system. *Environmental Research Letters*, *13*(11), 1–13.

Jones, B., Bull, D., Farquharson, L., Buzard, R., Arp, C., Grosse, G., & Romanovsky, V. (2018b). A decade of annual permafrost coastal observations indicate changes in the arctic system. *Environmental Research Letters*, *13*(11), 1–13.

Jones, B. M., Arp, C. D., Jorgenson, M. T., Hinkel, K. M., Schmutz, J. A., & Flint, P. L. (2009). Increase in the rate and uniformity of coastline erosion in arctic alaska. *Geophysical Research Letters*, *36*(3).

Jones, B. M., Hinkel, K. M., Arp, C. D., & Eisner, W. R. (2008a). Modern erosion rates and loss of coastal features and sites, beaufort sea coastline, alaska. *Arctic*, 361–372.

Jones, B. M., Hinkel, K. M., Arp, C. D., & Eisner, W. R. (2008b). Modern erosion rates and loss of coastal features and sites, beaufort sea coastline, alaska. *Arctic*, 361–372.

Jones, B. M., Irrgang, A. M., Farquharson, L. M., Lantuit, H., Whalen, D., Ogorodov, S., ... others (2020). Coastal permafrost erosion. *Arctic report card*, *15*.

Kamalov, A., Ogorodov, S., Birukov, V. Y., Sovershaeva, G., Tsvetsinsky, A., Arkhipov, V., ... Solomatin, V. (2006). Coastal and seabed morpholithodynamics of the baydaratskaya bay at the route of gas pipeline crossing. *Kriosfera Zemli (Earth Cryosphere)*, *10*(3), 3–14.

Kobayashi, N. (1985). Formation of thermoerosional niches into frozen bluffs due to storm surges on the beaufort sea coast. *Journal of Geophysical Research: Oceans*, *90*(C6), 11983–11988.

Kobayashi, N., Vidrine, J., Nairn, R., & Soloman, S. (1999). Erosion of frozen cliffs due to storm surge on beaufort sea coast. *Journal of coastal research*, 332–344.

Landrum, L., & Holland, M. M. (2020). Extremes become routine in an emerging new arctic. *Nature Climate Change*, *10*(12), 1108–1115.

Lantuit, H., Overduin, P. P., Couture, N., Wetterich, S., Aré, F., Atkinson, D., ... others (2012). The arctic coastal dynamics database: a new classification scheme and statistics on arctic permafrost coastlines. *Estuaries and Coasts*, *35*(2), 383–400.

Longuet-Higgins, M. S. (1970). Longshore currents generated by obliquely incident sea waves: 1. *Journal of geophysical research*, *75*(33), 6778–6789.

Miles, J. W. (1957). On the generation of surface waves by shear flows. *Journal of Fluid Mechanics*, *3*(2), 185–204.

Nielsen, D., Pieper, P., Barkhordarian, A., Overduin, P., Ilyina, T., Brovkin, V., ... Dobrynin, M. (2021a). Projected increase of arctic coastal erosion and its sensitivity to warming in the 21st century.

Nielsen, D., Pieper, P., Barkhordarian, A., Overduin, P., Ilyina, T., Brovkin, V., ... Dobrynin, M. (2021b). Projected increase of arctic coastal erosion and its sensitivity to warming in the 21st century.

Ogorodov, S., Aleksyutina, D., Baranskaya, A., Shabanova, N., & Shilova, O. (2020). Coastal erosion of the russian arctic: An overview. *Journal of Coastal Research*, *95*(SI), 599–604.

Ogorodov, S., Arkhipov, V., Kokin, O., Marchenko, A., Overduin, P., & Forbes, D. (2013). Ice effect on coast and seabed in baydaratskaya bay, kara sea. *Geography, Environment, Sustainability*, *6*(3), 21–37.

Overeem, I., Anderson, R. S., Wobus, C. W., Clow, G. D., Urban, F. E., & Matell, N. (2011a). Sea ice loss enhances wave action at the arctic coast. *Geophysical Research Letters*, *38*(17).

Overeem, I., Anderson, R. S., Wobus, C. W., Clow, G. D., Urban, F. E., & Matell, N. (2011b). Sea ice loss enhances wave action at the arctic coast. *Geophysical Research Letters*, *38*(17).

Overeem, I., Anderson, R. S., Wobus, C. W., Clow, G. D., Urban, F. E., & Matell,

N. (2011c). Sea ice loss enhances wave action at the arctic coast. *Geophysical Research Letters*, *38*(17).

Phillips, O. M. (1957). On the generation of waves by turbulent wind. *Journal of fluid mechanics*, *2*(5), 417–445.

Ravens, T., Jones, B., Zhang, J., Arp, C. D., & Schmutz, J. A. (2012). Process-based coastal erosion modeling for drew point, north slope, alaska. *Journal of Waterway, Port, Coastal, and Ocean Engineering*, *138*(2), 122–130.

Ravens, T., Ulmgren, M., Wilber, M., Hailu, G., & Peng, J. (2017). Arctic-capable coastal geomorphic change modeling with application to barter island, alaska. In *Oceans 2017-anchorage* (pp. 1–4).

Rodrigues, J. (2008). The rapid decline of the sea ice in the russian arctic. *Cold Regions Science and Technology*, *54*(2), 124–142.

Roelvink, D., Reniers, A., Van Dongeren, A., Van Thiel de Vries, J., Lescinski, J., & McCall, R. (2010). Xbeach model description and manual. *Unesco-IHE Institute for Water Education, Deltares and Delft University of Tecnhology. Report June*, *21*, 2010.

Rolph, R., Overduin, P. P., Ravens, T., Lantuit, H., & Langer, M. (2021). Arcticbeach v1. 0: A physics-based parameterization of pan-arctic coastline erosion. *Geoscientific Model Development Discussions*, 1–26.

Rowland, J., Jones, C., Altmann, G., Bryan, R., Crosby, B., Hinzman, L., . . . others (2010). Arctic landscapes in transition: responses to thawing permafrost. *Eos, Transactions American Geophysical Union*, *91*(26), 229–230.

Russell-Head, D. (1980). The melting of free-drifting icebergs. *Annals of glaciology*, *1*, 119–122.

Saha, S., Moorthi, S., Wu, X., Wang, J., Nadiga, S., Tripp, P., . . . others (2014). The ncep climate forecast system version 2. *Journal of climate*, *27*(6), 2185–2208.

Serreze, M., Barrett, A., Stroeve, J., Kindig, D., & Holland, M. (2008). The emergence of surface-based arctic amplification. *The Cryosphere Discussions*, *2*(4), 601–622.

Squire, V. A., Vaughan, G. L., & Bennetts, L. G. (2009). Ocean surface wave evolvement in the arctic basin. *Geophysical Research Letters*, *36*(22).

Steele, M., Ermold, W., & Zhang, J. (2008). Arctic ocean surface warming trends over the past 100 years. *Geophysical Research Letters*, *35*(2).

Stein, R., Fahl, K., Fiitterer, D., Galimov, E., & Stepanets, O. (2003). River run-off influence on the water mass formation in the kara sea. *Siberian Rer Run-Off in the Kara Sea: Characterisation, Quantification, Variability and Environmental Significance*, 9.

Stroeve, J., & Notz, D. (2018). Changing state of arctic sea ice across all seasons. *Environmental Research Letters*, *13*(10), 103001.

SWAN. (2021). *Simulating waves nearshore.* `https://swanmodel.sourceforge.io/`.

White, F. M., Spaulding, M. L., & Gominho, L. (1980). *Theoretical estimates of the various mechanisms involved in iceberg deterioration in the open ocean environment.* (Tech. Rep.). USA: RHODE ISLAND UNIV KINGSTON.

Appendix A Appendix

A1 Four zones of the coastal profile

The four zones of the Arctic coast in terms of erosion, thermal energy transfers and involvement of various physical processes are described in the Figure:4. The four zones are defined as follows:

1. **bluff surface**: it is the surface behind the cliff point X_c. The slope in the zone is zero or close to zero. The surface is covered with vegetation during the summer. Subsidence due to the thawing of the permafrost is the major change in the profile. Thawing depth is dependent on the convection of air and solar radiation. We assume the erosion due to surface run-off is negligible (based on field observation). The bluffs are usually filled with ice-wedge polygons. The organic-active layer at the top of the surface has negligible shear strength but can contribute to the lower erodibility to surface run offs.
2. **bluff face**: It is the steepest slope of the profile, in between the base point X_b and cliff point X_c and the most active part of the profile. The thawing process contributes directly to the mass loss by slumping and cliff retreat.
3. **beach**: The narrow beach in front of the bluff from the base point X_b to the swash point X_s. The thawed sediments accumulate on the beach. The collapsed bluffs fall on the beach. The beach is subject to inundation during the summer storms. The return currents created during the storms sort out the accumulated sediments and transport them towards offshore.
4. **seabed**: It is defined from the swash point X_s to the offshore. The general direction of the sediment transport is towards offshore since there exist no restoration mechanisms at the Arctic beaches. The wave induced particle movement is enough to transfer heat (convective heat transfer). The thawing depth is not the limiting factor, i.e. the permafrost lies quite deep. However, due to sea ice, the sediment transport during the winter is negligible.

A2 Definitions

Below are some geometric parameters defined to explain the Arctic coasts:

1. profile line: the surface line of the beach profile not including the snow or ice-sheets. During the summer, the profile line is exposed to the environmental parameters.
2. permafrost line or P-line: the melting face of the permafrost. During the winter, the line is assumed to be collided with the profile line. The difference between the beach line and permafrost line is the thawing depth.
3. base point: the point at the end of the beach where a sudden change in the slope occurs. Typically it stands above the tidal range and in calm conditions water level can not reach the base point.
4. cliff point: the end of the bluff-face and beginning of the bluff-surface; a sudden change in the slope.
5. ice-wedge top point: the point at the surface where ice-wedge polygon is visible on the surface.
6. ice-wedge bottom point: not necessarily the bottom point of the ice-wedge. It is the point from where we can assume the continuity of the bluff is broken by the ice-wedge.
7. swash point/line: Where the average water depth for a timestep is less than 5cm. The point(1D) or line(2D) is assumed to be constant for one timestep.
8. thawing depth: The difference between the permafrost line and profile line, calculated for the grid points on the profile line and normal to the tangent on the point at the profile line.

A3 Numerical schematisation of the submodules

A31 Modelling storm surge

Storm surge is modelled by discretising the Eq.1. The setup/surge level η is assumed to be zero at the offshore boundary, where η is the water level setup from the mean sea level. The surge level, η is determined at a 3-hour interval. The 3-hour time-averaged wind speed is used as an input parameter. When the ice concentration near the sea, i_{con} is above 20%, the surge is set to zero, assuming damping from the ice. The following equation determines the storm surge at each grid point.

$$\eta_{i-1} = \eta_i + \frac{f v_i \Delta x}{g} + \Delta x \frac{C_f U_i^2}{g\left(h_i + \eta_i\right)} \tag{A1}$$

A32 Modelling slumping

The numerical schematisation of slumping is shown in the Figure:A1. Part of the profile line ABCD is shown; the P-line WXYZ has varied thawing depth for a particular time step. The module, when activated, checks if the slumping is triggered at each grid point.

Let us assume, at the particular timestep, the module is checking whether slumping is triggered at point B. Using the critical slope criteria mentioned in Eq.7, we develop a slumping module based on the following assumptions:

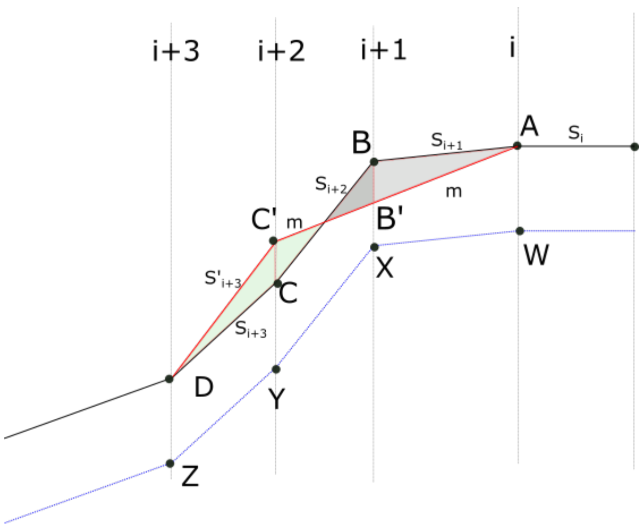

Figure A1: The numerical shcematization of slumping based on critical slope and fall by gravity only. The line ABCD is the profile line which had WXYZ permafrost line at various thawing depth of each grid points. The slope at point B is greater than m_a which triggers the slumping and the new position for the point B at the same grid line is B'

- The slumping process is initiated by gravitational force only. We ignore the water flow created by the thawing of permafrost.
- the conditions for the initiation of the slumping are as follows:
  1. No slumping occurs at the permafrost line, the line WXYZ, irrespective of the slope at the grid lines.

2. The slope at the grid point before the concerned cell has a lower slope than critical. In the Figure:A1, when we consider if the slumping is triggered at point B, the slope of the line AB; S_{i+1} must be lower than m_a.

3. the slope at the concerned grid point must satisfy the Eq.xx,i.e. the slope of line BC (S_{i+2}) is greater than m_a.

4. For each iteration, the mass transfer is limited to two adjacent grid cells; the mass balance is maintained.

5. As a result of slumping, the grid point in consideration, point B, will be subsided to B', which will increase the elevation of point C to C'.

6. In Figure, point B: the subsidence of the concerned point will be such that the area under the curve ABCD will be equal to the area AB'C'D. This rule is overridden when the subsidence of point B' is limited by the permafrost line. Point B is not allowed to be lowered than point X.

- The slumping process is always triggered in the downward direction,i.e. for a particular time step, if two grid points have a slope more than the critical value, m_a, slumping will be initiated at the grid point in the higher vertical position.
- There is no limit of the iterations for each time step, i.e. the module will run until all the grid points in the profile satisfy the governing equation.
- The module runs at each timestep. If the slumping occurs, it over-rides the thawing depth, x_t estimated by the thawing depth modules.

Modelling bluff stability

Four mode of failure cases are considered at each timestep. Three of them is the shear failure (mode#1 to#3) and the rest moment failure, the governing equations are described earlier. The failure modes are as follows(see Figure:A2):

1. model#1: The failure line is CE (from the cliff point to the base point E). The bluff face got steeper as a result.
2. mode#2: The failure line is GE. The point G is determined using the same slope of the bluff.
3. mode#3: The failure line is FE. F is the lowest point of the ice wedge polygon. The shear failure line is the FE.
4. model#4: The failure line is PE and PF. This is the moment failure mode.

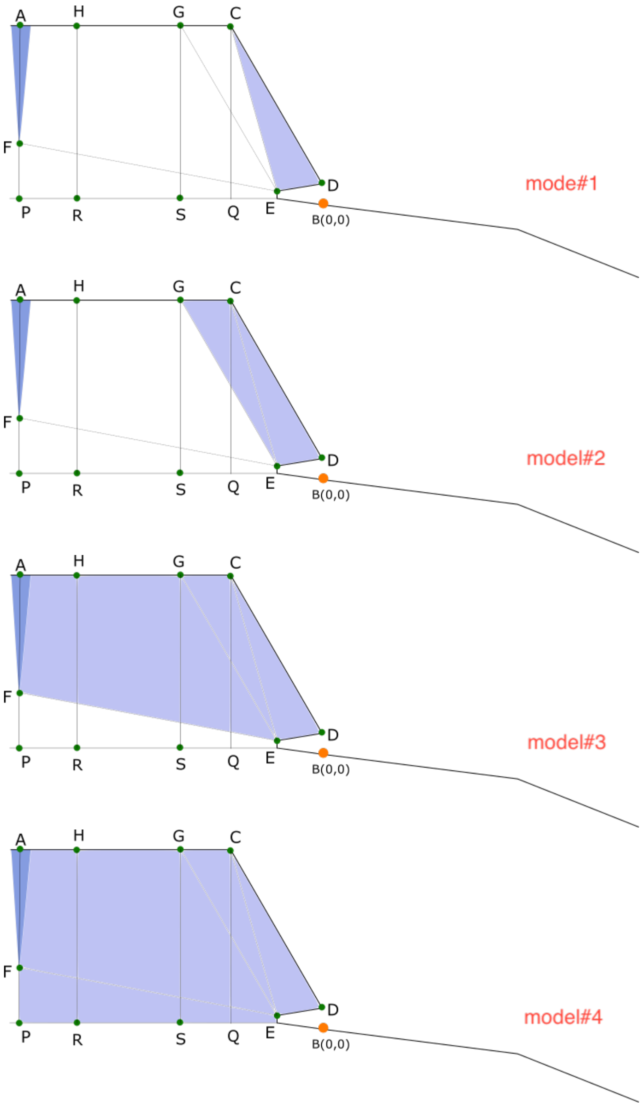

Figure A2: The stability of the overhanging bluffs

Timesteps

The hydrodynamic modules of XBeach are used to simulate 3 hours of the hydrodynamic forcing as shown in the Figure:9. We chose 3 hours as our global timestep as sea-state is described at 3-hour intervals. Some of the global parameters, like wind speed, air temperature etc are used as input for various modules. Storm surge, tide and wave near the shore (500 metres from the swash zone) are used as input for the XBeach.